NUMERICAL SIMULATION OF THREE-DIMENSIONAL TSUNAMI GENERATION BY SUBAERIAL LANDSLIDES

A Thesis

by

GYEONG-BO KIM

Submitted to the Office of Graduate Studies of
Texas A&M University
in partial fulfillment of the requirements for the degree of

MASTER OF SCIENCE

Approved by:

Chair of Committee,	Juan J. Horrillo
Committee Members,	Moo-Hyun Kim
	Ayal Anis
Department Head,	John Niedzwecki

December 2012

Major Subject: Ocean Engineering

ABSTRACT

Tsunamis are one of the most catastrophic natural events impacting coastal regions often generated by undersea earthquakes. Nevertheless, in enclosed basins, *i.e.*, fjords, reservoirs and lakes, subaerial or submarine landslides can initiate devastating tsunamis with similar consequences. Although a subaerial or submarine landslide that impinges into a large water body can generate a tsunami, subaerial landslides are much more efficient tsunami generators than its counterpart. In this study we aim to integrate laboratory scale experiments of tsunami generation by subaerial landslide with numerical models. The work focuses on the numerical validation of two three-dimensional Navier-Stokes (3D-NS) models, FLOW-3D and our developed model TSUNAMI3D. The models are validated based on previous large scale laboratory experiments performed by a tsunami research team lead by Dr. Hermann Fritz, Georgia Institute of Technology. Three large scale landslide scenarios were selected from the set of laboratory experiments, namely, fjord like, headland and far field coastline. These scenarios showed that complex wave fields can be generated by subaerial landslides. The correct definition and evolution of the wave field are key to accurate modeling the ensuing tsunami and its effect in coastal regions. In this study, comparisons are performed between numerical results and laboratory experiments. Methodology and key parameters for soil rheology are defined for model validations. Results of the models are expected to be under the allowable errors indicated by the National Tsunami Hazard Mitigation Program (NTHMP), National Oceanic and Atmospheric Administration (NOAA) guidelines for validation of tsunami numerical models. The ultimate goal of this research is to obtain better tsunami calculation tools for real-world application of 3-D models for landslide tsunamis, which are neces-

sary for the construction of inundation maps in the Gulf of Mexico and the Caribbean regions.

DEDICATION

This work is dedicated to my wife,

Mrs. Mi-Hyang Oh,

and to my child,

Brayden Hangyul Kim,

without whose love and support this work would have not been possible.

ACKNOWLEDGEMENTS

First and foremost, I would like to express my sincerest thanks to my advisor, Dr. Juan Horrillo, for his continuous support throughout my academic career at Texas A&M. From the beginning of my graduate studies, he has provided me with endless opportunities, significantly contributing to my academic and professional development. His insight, kindness, and contagious enthusiasm have truly inspired me in a way that I will never forget.

I would also like to thank my thesis committee members, Dr. Moo-Hyun Kim and Dr. Ayal Anis, for their time and contributions in reviewing this work.

I am very grateful to Dr. Hermann Fritz, Dr. Mohammed Fahad, and Mr. Brian McFall in Georgia Institute of Technology for their contributions and for taking time to support their experimental data on this exciting project. Without this opportunity a large portion of this work would have not been possible.

I extend sincere thanks to Dr. Namhyeong Kim, who was my advisor in Korea for prayers and his encouragement and wisdom. In addition, I thank all of my fellow graduate students and friends: Haengsik, Daehyun, Sungwon, Yoonsook, Taeho, Heeju, Chankweon, Kyungsung, Heonyong, Abhisheck, Lei, Ashwin, and Gaurav at Texas A&M for their love and support during the past two years.

Finally, I want to express my utmost appreciation to my family for all of the prayers and love they have provided for me during my life. Without you, none of this would be possible.

NOMENCLATURE

F	Froude number
α	slope angle
h	still water depth
s	slide thickness
w	slide width
b	slide width
l_s	slide length
V_s	slide volume
v_s	slide velocity
v_b	landslide release velocity from the slide box
ρ_s	slide density
ρ_w	water density
R_u	maximum runup
R_d	minimum runup
n	porosity
g	acceleration due to gravity
$rorx$	radial propagation distance from impact region
θ	propagation direction
t	time
a_M	maximum amplitude
H_M	maximum wave height
c	wave celerity
β	opposite slope angle

φ	internal friction angle
δ	basal slide friction
d_{50}	mean grain size
m_s	landslide mass
G	specific gravity
M	dimensionless landslide volume
X	dimensionless distance(x/h)
R	dimensionless distance(r/h)
S	dimensionless landslide thickness
T_s	dimensionless underwater travel time
Σ	dimensionless landslide front area (ws/h^2)
p	pressure
ν	kinematic viscosity
t^m	old time

NTHMP	National Tsunami Hazard Mitigation Program
NOAS	National Oceanic and Atmospheric Administration
NEES	Network for Earthquake Engineering Simulation
CFD	Computational Fluid Dynamic
3D-NS	Three-dimensional Navier-Stokes
FDM	Finite Difference Method
VOF	Volume of Method
FAVOR	Fractional Area Volume Obstacle Representation
DNS	Direct Numerical Simulation
PIV	Particle Image Velocimetry
STL	Stereo-lithography
SCS	Suspended concentration sediment
ERR	Normalized error

TABLE OF CONTENTS

LIST OF FIGURES

LIST OF TABLES

TABLE Page

1. INTRODUCTION

1.1 Background

Tsunamis are one of the most catastrophic natural events impacting coastal regions, usually generated by undersea earthquakes, landslides, rocks falls, volcanic eruptions, large-scale gas hydrate emissions and possibly by asteroid impact. In enclosed basins, *i.e.,* fjords, reservoirs and lakes, subaerial or submarine landslides can initiate devastating tsunamis by transferring its potential energy to the water body. The transfer of energy is manifested by relatively short but large impulsive disturbances on the free water surface. Recently, the study of landslides generated by impulsive water waves has greatly increased due to major natural disasters caused by this phenomenon. One of these dramatic events occurred in 1958 at Lituya Bay, Alaska (Miller, 1960; Fritz et al., 2001, 2009), when a subaerial landslide triggered by an earthquake entered into the water at the Gilbert Inlet and generated a massive impulsive wave (Miller, 1960). The resulting wave runup was the highest known in tsunami history; the water rose up 524 m at the slope located in front of the landslide, then the waves propagated into the bay and eventually radiated offshore through the bay inlet with minimum effects outside the bay as shown in Fig. 1.1. Another case related to submarine landslide is the Papua New Guinea event, (Tappin et al., 2001; Synolakis et al., 2002), which was generated by an underwater slump movement triggered by a magnitude 7 earthquake in 1998. The tsunami wave struck about 30 km of coastal shoreline with a maximum runup of about 15 m, killing over 2100 people. These events had served as the prelude for advanced landslide tsunami investigations. Landslide generated impulse waves can occur not only at the coastline and offshore, but also in enclosed basins (*i.e.,* reservoir and lakes). The event

(a)

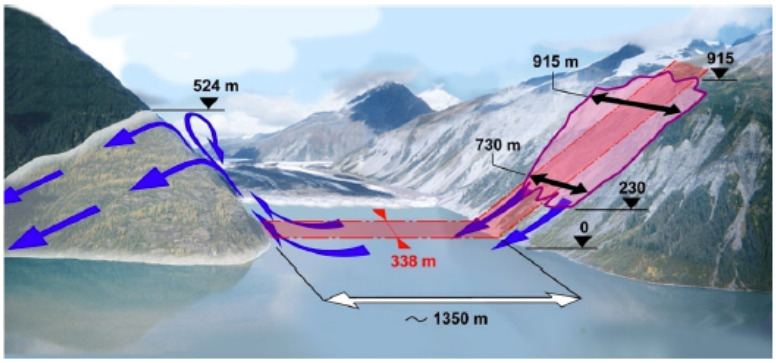

(b)

Figure 1.1: The 1958 Lituya bay landslide tsunami event: (a) trim-line of the tsunami runup measured from the destroyed vegetation and (b) maximum recorded tsunami runup of 524 m in the direction of landslide prolongation Miller (1960); Fritz et al. (2001, 2009)

that took place at the Vajont Valley in Italy on 1963 is perhaps the more disastrous one. A subaerial landslide of about 270 million cubic meters fell into the Vajont reservoir and generated impulse waves that ran up to about 235 m. The large wa-

ter waves overtopped the concrete arc dam, then flooded the village of Longarone, and finally ended 1901 lives (Müller, 1964; Panizzo et al., 2005a). Although often generated in the open ocean, the effects of tsunamis are mostly confined to coastal areas. A tsunami may damage coastal structures such as breakwaters, seawalls, piers, bridges/pillars, artificial floating island/airport and even fish and wind farms (Silva et al., 2000). In addition to their threat to human communities and vital infrastructure, landslides generated tsunami also menaces installations of offshore structures such as platforms, risers, FPSO, pipelines and subsea systems such as manifolds on the continental shelf and slope (Swanson and Jones, 1982; Bruschi et al., 2006). While the mechanism for generation of the initial water waves by purely tectonic motions from earthquake is reasonably well understood, the understanding of landslide generated waves is marginal. More in details, landslide generated tsunami events are commonly classified as three categories based on the initial position of the landslide relative to the water body as shown in Fig. 1.2. These are

- Subaerial landslides generated tsunamis involve all the three phases of air, water and slide materials. This is concerned with the subaerial landslide motion, impact of landslide on the water surface and the submarine debris runout and deposition. In general, the wave train starts as an elevation. The tsunami wave heights tend to decrease with increasing submergence of the initial position of the landslide.

- Partially submerged events also involve all the three phases.

- Submarine landslides generated tsunamis can be treated as two phase flow considering only the slide material and water. In this case, the initial landslide position is fully submerged underwater. Usually, the wave train begins with a depression or a trough.

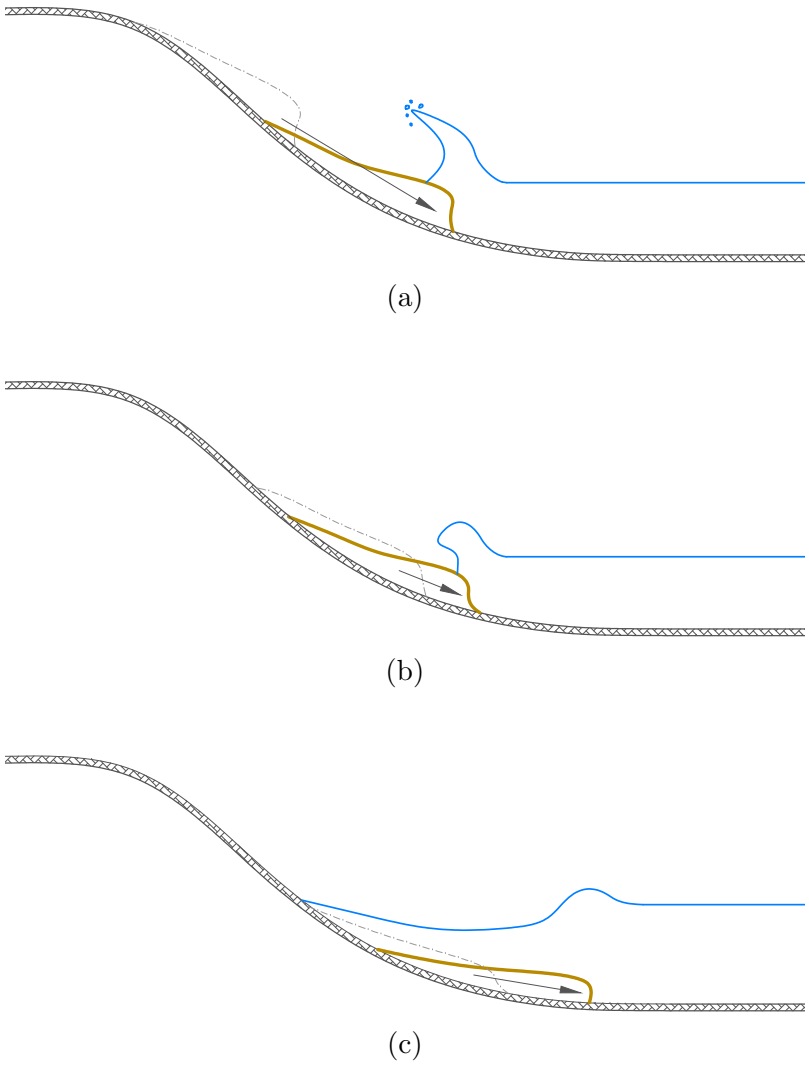

Figure 1.2: Classification of landslide generated tsunami base on the initial position of the landslide: (a) subaerial; (b) partially submerged; and (c) submarine or subaqueous.

This classification is commonly used for observations and describing the landslide generated tsunami models(Mohammed, 2010). As described above, the initial position of the landslide determines the characteristics of the generated tsunami and the importance of air as the third phase. The tsunami wave heights tend to decrease with increasing submergence of the initial position of the landslide.

Landslide generated tsunamis can occur either in coastal areas or in closed water basins such as bays and lakes. Further, submarine landslide generated tsunamis can occur offshore where the continental shelf breaks. While either a subaerial or submarine landslide that impinges into a large water body can generate a tsunami, subaerial landslides are much more efficient tsunami generators than the slower submarine landslides (Koo and Kim, 2008).

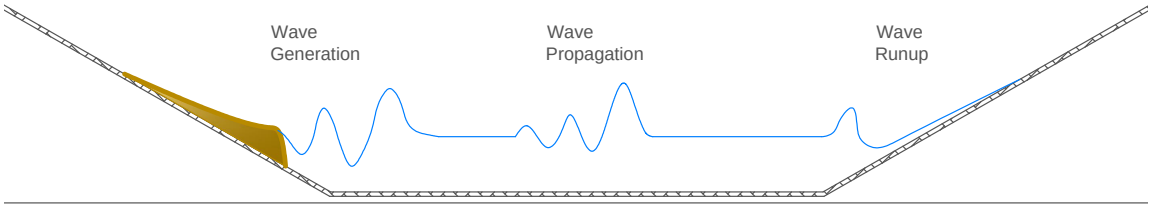

Figure 1.3: Phases of landslide generated tsunamis: wave generation, propagation and runup

The landslide tsunami process involves the landslide motion, tsunami wave generation, landslide runout, tsunami propagation and runup shown in Fig. 1.3. When the landslide reaches the free surface, a wave is generated and landslide energy is transferred to water. The induced waves quickly leave the generation area and propagate in the near field. The near field features of such an impulse wave depend upon the characteristics of the landslide source (*e.g.,* volume, velocity, density, porosity, shape of the front, slope angle, etc.). Then the waves propagate in the far field where frequency and directional energy dispersion, refraction, reflection and diffraction occur, depending upon water body configuration and waves features. Finally, the wave reaches the water body boundaries and it runs up and floods coastal areas, often resulting in great damage and danger for human activities (Di Risio et al., 2011, chap. 6).

1.2 Motivation and Scope of Present Study

Tsunamis generated by landslides may pose perceptible tsunami hazards to areas regarded as coastal and offshore area and confined water bodies such as bays, fjords, lakes, rivers, and reservoirs. The effects of a tsunami generated by landslide along a coast can generate a devastating local impulsive wave affecting the surrounding region. To mitigate tsunami coastal hazards, the first step is to identify the tsunami inundation zone, *i.e.,* the coastal zone at higher tsunami risk. Such a task is achieved by using numerical models, consulting historical records or by conducting geologic and geomorphology studies to detect past tsunami events. In area where the maximum potential tsunami source is known *i.e.,* areas with active landslides, tsunami generation mechanisms, initial wave configuration, propagation, and runup can be mathematically modeled and maximum tsunami wave heights and runup can be estimated. To ensure a better and reliable prediction in tsunami generation and runup regions, it is essential to use tsunami calculation tools from different perspectives to study the tsunami properties: (a) the mechanism of tsunamigenic landslides; (b) the tsunami wave generation in the near field region; (c) the tsunami wave propagation; (d) the hazards associated with tsunami wave runup and impact. For practical applications such as construction of inundation maps, numerical models for tsunami predictions are also needed to be tested over a variety of benchmark problems from analytical formulations and experimental data of field measurements to ensure the matching model results expected values within a minimum margin of error. Furthermore, tsunami models need to be continuously tested with any new set of laboratory data or tsunami field data that becomes available, Synolakis et al. (2007).

This study therefore aims to integrate laboratory-scale experiments of tsunami generation by subaerial landslide with numerical models. The work focuses on the

numerical validation of two 3-D Navier-Stokes (3D-NS) models, FLOW-3D and our developed model TSUNAMI3D. The validation of the models relies on recent laboratory experiments carried out by the Georgia Institute of Technology, Dr. Hermann Fritz, in Oregon State University Mohammed et al. (2011). The experimental results showed that complex wave fields can be generated by subaerial landslides. The correct definition and evolution of the wave fields near the landslide source are key to modeling of the ensuing tsunami and determining its effects in coastal regions, mainly for tsunami hazard mitigation purposes. The set of laboratory experiments comprises 3-D subaerial-deformable granular landslides and each of them are implemented for several physical-large-scale domain configurations such as fjord-like, headland and far field coastline. The modeling tasks consist of reproducing tsunami waves numerically generated by these large-scale-landslide scenarios. Both models are fully 3-D and able to consider soil rheology on very complex domain geometry.

As a first stage of this work, the 3D-NS models were used to help in the construction process of the physical experiments, for example: (a) to determine efficient physical layouts for experiment setups to achieve the best performance of the physical-scale models. This task facilitated the determination of the most efficient basin geometry within a given water depth, *i.e.,* avoiding gauge noises due to wave reflection; (b) to re-examine laboratory experiment results and facilitate physical model setups for specific requirements, *e.g.,* changing location of the landslide source generator to obtain a reproducible pattern of wave signals. Finally, the set of data obtained from the large-scale-landslide scenarios are used to conduct validation and verification of the numerical models, TSUNAMI3D and FLOW-3D. Comparisons are performed between numerical results and laboratory experiments. It is expected that results of the models will be under the allowable errors indicated by the National Tsunami Hazard Mitigation Program (NTHMP), National Oceanic and Atmospheric

Administration (NOAA) guidelines for the validation of tsunami numerical models. The ultimate goal of this research is to obtain better tsunami calculation tools for real-world application of 3-D model to landslide tsunami, which are necessary in the construction of inundation maps in the Gulf of Mexico and the Caribbean regions. The hope of this proposed study in the near future is the mitigation of the devastating consequences of tsunami events, including loss of human life, destruction of property, damage to the environment and economic and social issues.

1.3 Literature Review

Tsunamis induced by landslides are one of the gravity water waves. These impulse waves are a response generated by an impulsive disturbance on the water body. Landslide driven tsunamis are presented by the parameters shown in Fig. 1.4. The landslide may be characterized by the slide thickness s, slide width b, slide length l_s, slide velocity at impact v_s, slide density ρ_s, the landslide front slope angle ϕ, water density ρ_w, still water depth h, hill slope angle α, maximum amplitude a_M, maximum wave height H_M, opposite slope angle β, the distance from impact point x, the wave celerity c. The waves η are defined as a function, $f(r, \theta, t)$, where r is the radial propagation distance from the origin relative to the landslide direction. The landslide direction corresponds to $\theta = 0^\circ$ while the lateral runup direction on the hill slope corresponds to $\theta = +90^\circ$ and -90°.

1.3.1 Physical Modeling of Tsunamis Induced by Landslides

The first experimental tasks were carried out by Russell (1838, 1845). He used a vertical falling box to generate free surface transient waves representing the large solitary elevation. The waves are induced by a sudden stop of a boat, as observed by Sir Scott Russell along a channel. The height of box was higher than the water depth. Later this impulse wave generation method was used by many researchers

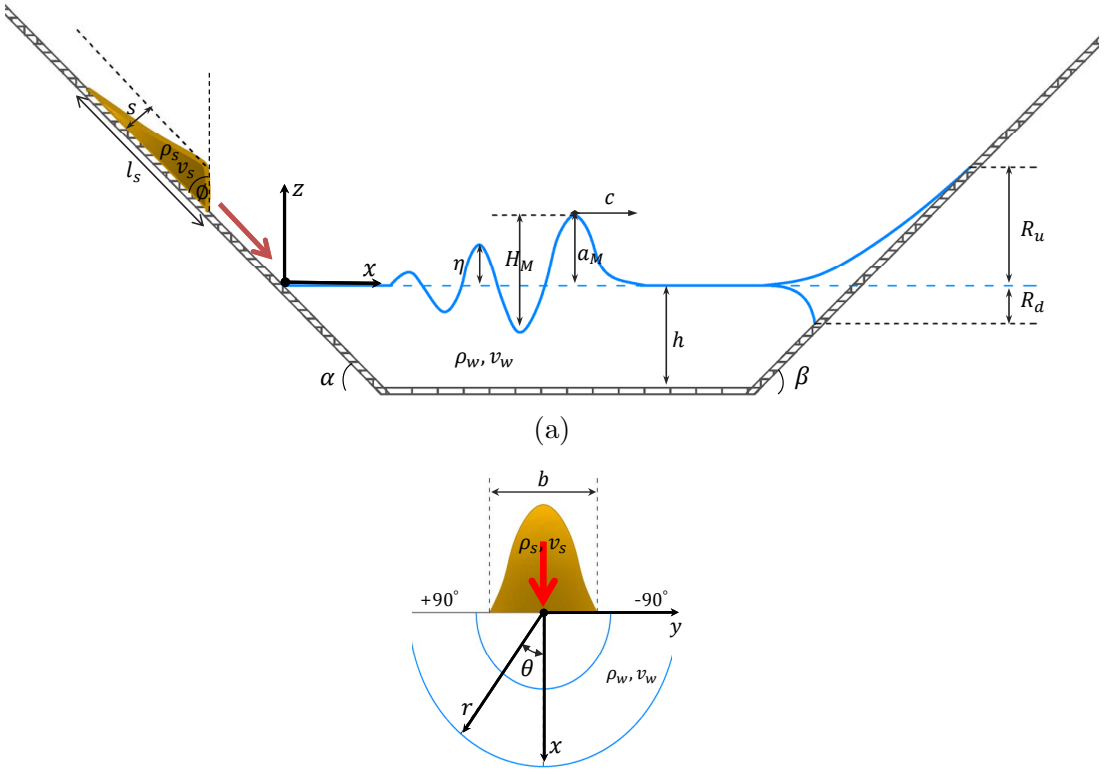

Figure 1.4: Sketch of a subaerial landslide-induced tsunami wave: (a) cross section defining parameters in the direction of slide motion; (b) plan view defining coordinate system to reference and quantify the generated tsunami wave

(*e.g.,* Wiegel et al. (1970); Noda (1970); Monaghan and Kos (2000)) and is often referred to as "Scott Russell's wave generator". Some researchers (*e.g.,* Panizzo et al. (2002); Di Risio (2005); Di Risio and Sammarco (2008); Yim et al. (2008)) used a falling box characterized by lower height of box than the water depth. Other studies were used to simulate the impulse wave generation by a landslide conducted by using either a vertical (*e.g.,* Noda (1970) or an inclined moving paddle (*e.g.,* Miller (1970); Iwasaki (1983)).

Wiegel (1955) used the Scott Rusell's wave generator to establish the wave profiles, fully submerged falling rigid bodies vertically and sliding down an inclines in tanks. Then Noda (1970) performed theoretical and experimental studies where the landslides are modeled as dropping a vertical box. He observed that the generated waves were classified based on Froude number, $F = v_s/\sqrt{gh}$ and the relative slide box thickness, where F the already defined landslide Froude number ($v_s/\sqrt{gh}$. Then he found that the higher density of the falling blocks, the higher the generated wave amplitudes. Later the Russell wave generator was also applied by Panizzo et al. (2002) as a pre-study for the 3-D models tests.

In the meantime, to investigate the characteristics of impact waves, a more useful fundamental parameters was analyzed by Kamphuis and Bowering (1970) based on their own experiments. The experiments consisted of a tray sliding down a slope. In this study, they proposed a simple dimensional analysis, by defining the relationships f between any dependent quantity (in dimensionless form, Π):

$$\Pi = f\left(F,\ M,\ G,\ X,\ T_s,\ \phi,\ \alpha,\ n\right), \tag{1.1}$$

where F the already defined landslide Froude number ($v_s/\sqrt{gh}$, v_s the landslide impact velocity, h still water depth), M the dimensionless 2-D landslide volume

($=V_s/wh^2$, V_s the landslide volume, w landslide width), G the specific gravity ($=\rho_s/\rho_w$, ρ_s the landslide bulk density, ρ_w water density), X the dimensionless propagation distance ($=x/h$, x the distance from impact point), t the time, g the gravitational acceleration, T_s the dimensionless underwater motion time ($t_s\sqrt{g/h}$), being t_s the underwater motion time, ϕ the landslide front slope, α the slope angle of the incline to horizontal, n the landslide porosity. Experimental investigation showed that the generated maximum wave height (H_M) is strongly affected by the dimensionless volume (M) and landslide Froude number (F). The leading wave period (T_l) is affected only by the dimensionless distance(X) as seen from Fig. 1.4a.

In the 3-D models, the generated tsunami waves are functions of the relative radial distance r/h and the angular direction away form the landslide direction θ as shown in Fig. 1.4b. The first 3-D physical investigation was performed by Huber (1980) with the aim of fully reproducing both deformations and porosity of landslide by employing a granular landslide model. He conducted roughly 150 times of 3-D experiments in a wave basin to estimate a reduction parameter capable of considering the 3-D effects due to lateral dispersion. It was observed that the landslide induced impulse waves in a water body propagate radially over the water surface. The radial spread of waves was characterized by the propagation direction θ (measured with respect to the direction of the landslide motion) and the radial travel distance r as shown in Fig. 1.4b. In this experiment, the wave height was at a maximum in the direction of the slide, and the wave decayed rapidly in the lateral direction. Then, Huber and Hager (1997) re-analyzed the same experimental data and a series of empirical formulation were defined, for 2- and 3-D water bodies. They observed that for 2-D water body, the main effect on wave height is related to the slope angle (α): the wave height decreased with decreased the slope angle. Additionally, the higher the dimensonless landslide volume (M) and specific gravity (G) and the

lower the dimensionless distance (X), the higher wave height. The 3-D effects for lateral dispersion were analyzed using a squared cosine function involving the wave propagation θ as below:

$$\frac{H_{max}}{h} = 1.76 \cdot sin\alpha \cdot cos^2\left(\frac{2\theta}{3}\right)\left(\frac{\rho_s}{\rho_w}\right)^{0.25} M^{0.5}\left(\frac{r}{h}\right)^{-2/3} \tag{1.2}$$

$$M = \frac{m}{bh^2\rho_s} = \frac{V_s}{bh^2} \tag{1.3}$$

where being b slide width , r the radial propagation distance from the origin.

More recently, as far as the granular slide models are concerned, some of 2-D experiments by using granular landslides with varying geometry and energy (*e.g.,* Fritz et al. (2001, 2003a,b, 2004); Zweifel et al. (2006); Heller et al. (2008); Heller and Harger (2010, 2011)). The experimental observations conducted with the aim to characterize the water flow in the near- and far field (Fritz et al., 2003a), as well as the impact crater features (Fritz et al., 2003b) and wave types (Fritz et al., 2004) with defining a series of empirical formulation. Heller et al. (2008) investigated the experimental task to analyze scale effects and the influence of slide mass and granulate characteristics on the tsunami waves. The 2-D experiments were carried out in a rectangular prismatic water channel which was 11 m long, 0.5 m wide and 1 m water depth. The landslide dynamics was controlled by means of a novel pneumatic landslide generator (Fritz et al., 2001). When comparing the materials between granular and solid type generated waves for subaerial landslide, Zweifel (2004) found that at least for 2-D study, solid blocks induce higher waves compared with granular materials. For 3-D physical investigation, Fritz et al. (2009) have reproduced the Lituya Bay event, and Mohammed et al. (2011) have studied the effects of different topographical and bathymetrical features for the three setup configurations: fjords,

headlands and farfield runup with deformable granular landslide sources. Although Fritz et al. (2004); Zweifel et al. (2006); Heller and Harger (2010) indeed performed different empirical formulations with varying experimental ranges and by considering several dimensionless groups: the influences of (a) landslide Froude number (F), (b) dimensionless landslide thickness (S=s/w, being the landslide thickness s measured perpendicular to the incline), (c) specific gravity (G), and (d) slope impact angle (α) are addressed: the higher the values of F, S, G, the higher the induced wave height and period; the lower the value of α (*i.e.,* less steep inclines), the higher the induced wave height and period. It should be mentioned that the influence of the slope impact angle seems to be opposed to the 3-D results found by Huber and Hager (1997) that observed increasing wave height for increasing α. In the case of subaerial landslides generated water motions, it is also possible to distinguish a slide impact zone, where splashes take place. It is worthwhile to mention splash zone studies to decay the induced wave height faster due to air entrainment, large turbulence production, amplitude dispersion and frequency dispersion, such as the experimental works of Fritz et al. (2001, 2003a,b), Walder et al. (2003); Hoque and Aoki (2008); Heller et al. (2008); Heller and Harger (2010), and the numerical simulations studied by Monaghan and Kos (2000), Mader and Gittings (2002, 2003); Gisler et al. (2006) and Panizzo et al. (2005b).

Other physical experiments were undertaken by using solid landslides. Walder et al. (2003) carried out on impulsive waves generated by subaerial mass flows. They proposed empirical formulations for the maximum generated wave height in the near field involving a scaling analysis of the Euler equation, and also demonstrated the influence of the landslide volume and the importance of the dimensionless underwater travel time $T_s(=t_s\sqrt{g/h})$, being under water motion time t_s. They found that the wave height increases while underwater travel time T_s decreases. Furthermore,

Walder et al. (2003) and Panizzo et al. (2005b) proposed some empirical formulations that the dimensionless underwater travel time value (T_s) is need:

$$T_s = 4.5\sqrt{L/h} \quad ; \quad T_s = t_s\sqrt{g/h} = 0.43\Sigma^{-0.27}F^{-0.66}(sin\alpha)^{-1.32}, \tag{1.4}$$

where L length of landslide block, h water depth, Σ the dimensionless landslide front area ($= ws/h^2$, being the landslide thickness s, the landslide width w). As introduced by Walder et al. (2003), the first equation of Eq. (1.4), should be used when landslide motion is mainly affected by frictional forces (*i.e.,* Coulomb friction) and hydrodynamic drag is less important (Savage and Hutter, 1989). Di Risio (2005) performed a series of 2-D experimental tests to provide empirical formulations by using a pseudo-Scott Russell's wave generator based on the dimensional analysis. They extended the work by Kamphuis and Bowering (1970) in Eq. (1.1) only for vertical landslides, *i.e.,* $\alpha = 90°$, and found that the higher the landslide Froude (F) and the shorter the relative dimensionless distance (X *or* $R = r/h$), being r the distance from impact point in 3-D water body and the dimensionless landslide thickness (S), the higher the maximum and leading wave height and crest amplitude. With respect to the wave period, it was found that it is slightly affected by the landslide Froude number.

For 3-D impulse wave generation, Panizzo et al. (2005b) used a tray sliding along a slope that generated impulse waves in a wave basin to describe the waves features while propagating both in the near- and far field. The generated wave types were classified based on a wavelet analysis approach with consideration on the dimensionless time of the landslide underwater motion (T_s). They studied that the generated wave height increases as the impact velocity of landslide (v_s) and the dimensionless landslide front area (Σ) increase. The directional wave energy distribution induces

smaller wave heights with respect to 2-D studies (Walder et al., 2003; Fritz et al., 2004). The 2-D experiments overestimated the relative amplitude by a factor of 5 to 10 as compared with their own data due to the difference of landslides between solid slides and deformable granular slides. In addition, they found that the wave height becomes greater as the incline slope (α) becomes smaller; on the contrary to the formulation by Huber and Hager (1997).

Enet and Grilli (2007) worked to confirm the importance of initial acceleration and terminal velocity of the sliding landslide. They found that when submarine landslides occur, a depression of free surface takes place above the initial region of the slide, and successfully validated the empirical formulation proposed by Watts et al. (2005).

Ataie-Ashtiani and Nik-Khah (2008) investigated to study the characteristics of impulse waves generated by subaerial landslides. They found that the landslide shape does not strongly affect the propagating wave height and then the energy exchanges from landslide into water body is generally increased by decreasing the landslide Froude number.

Di Risio et al. (2009) performed a 3-D experiment which was similar to the cases simulated by Lynett and Liu (2005) with the aims to observe the nearfield wave and the propagation alongshore of the leading wave. In this study, the secondary runup peak was located and the maximum runup was located at about two times the landslide width away from the centerline of the landslide rather than directly landword the landslide. Both partially submerged and subaerial landslide were reproduced.

1.3.2 Numerical Modeling of Tsunamis Induced by Landslides

Many numerical studies of tsunamis induced by landslide have been performed on a variety of models and hypotheses with respect to slide motion and geometry.

Jiang and LeBlond (1992, 1993) conducted a numerical simulation to study deformable mudslide and water motion for the surface waves generating by depth-averaged nonlinear shallow water equations for both water waves and mudslide. This approach was applied by other authors (*e.g.,* Harbitz et al. (1994); Imamura and Imteaz (1995); Imteaz and Imamura (2001); Heinrich et al. (2001)) to describe underwater landslide tsunamis. However, even though the shallow water equations are relatively accurate in many practical tsunami simulations, it is still doubtful when this approach is applied to landslide tsunamis due to the neglecting vertical accelerations in the nonlinear shallow water wave equations. More in details, the landslide generated waves usually fit in the intermediated water wave regime, where vertical fluid velocity and accelerations are important for the wave dynamic. This physical aspect on the wave dynamic is even more critical during the initiation of the landslide motion or tsunami generation being to most subaerial cases (Fritz, 2002; Grilli et al., 2002; Kowalik et al., 2005a).

In the meantime, Heinrich (1992) conducted numerical studies on tsunamis generated by landslides using the NASA-VOF2D model with a Volume of Fluid (VOF) method to describe behavior of rigid blocks, then later developed a 3-D model. The model was a nonlinear Eulerian model which solves the fully Navier-Stokes equations by a finite difference method. Either subaerial or submarine landslide and bottom movement were allowed in this model. He developed a shallow water numerical model to clarify the efficiency of deep slumps in generating tsunami waves.

Assier-Rzadkiewicz et al. (1997) simulated an underwater landslide using a 2-D fluid mechanics mixture model based on Navier-Stokes equations. The free surface motion was represented by a VOF method and the sediment (*i.e.,* mud) was considered as a viscoplastic fluid, with rheological parameters, *e.g.,* the diffusion and viscosity coefficients, the Bingham yield stress and the basal friction. The model

was well validated with analytical solution and laboratory experiments (Heinrich, 1992) for a viscous-Bingham flow and tested for a rigid box and gravel slide. They stressed out the importance of the sediment rheology and the diffusion parameter.

Later Monaghan and Kos (2000) used 2-D numerical particle model, soothed particle hydrodynamics (SPH) with described in Monaghan (1992), to clarify the details of the wave formation and the box dynamics associated with the Scott Russell's wave generator. They found that as the box sinks, a jet water from below raise up to generate a reverse plunging wave and the forward solitary wave forming a vortex, involving breaking waves and air bubbles entrapment during cavity collapse. The numerical results overestimated the experimental results by 3 %-18 % depending on the initial water depth.

Watts et al. (2000) developed a numerical model to describe the water waves generated by underwater landslides and compared them with the experimental results. In this study, the depth averaged nonlinear shallow water equations were used to simulate tsunamis, and the model appeared to underestimate the wave amplitude. The slide was modeled as a block of semi elliptical cross-section. Later, Watts et al. (2003) simulated tsunami propagation and inundation using GEOWAVE by combining the nonlinear Boussinesq long wave propagation model FUNWAVE to simulate an arbitrary tsunami initial bathymetry condition and the TOPIC (Tsunami Open and Progressive Initial Condition Systems). They discussed that nonlinear and dispersive tsunami propagation models may be necessary for modeling submarine mass failure (SMF) cases, *i.e.,* underwater slides and underwater slumps.

As for potential flow models, Grilli and Watts (1999) and Grilli and Watts (2005) applied fully nonlinear 2-D and 3-D potential flow (Boundary Element Method (BEM)) simulations of underwater landslide tsunamis to water wave generation. They assumed geometrically idealized landslide shape *i.e.,* for the 2-D a semi-ellipse

or bump configuration and for the 3D a bi-Gaussian-shaped or saucer configuration. The landslide center of mass motion sliding on the slope was prescribed based on a dynamic force balance using Newton's laws and some empirical coefficients based on theories or validated experimentally. However, in this study, they could not simulate the shear forces acting on the front and the top of the slide for underwater slide.

Other well known numerical model referred as the multi-phase models is the SAGE hydro code. SAGE has been used in many occasion by modelers to simulate landslide induced tsunami, Mader and Gittings (2002, 2003) and Gisler et al. (2006). The code, originally developed by Gitting (1992) for Science Applications International, Los Alamos National Laboratory, is mainly suited in compressible multi-material simulations, *e.g.,* meteorite impact, Gisler et al. (2004). It solves the full set of compressible Navier-Stokes equations, including the equation of state and different constitutive models for material strength. An automatic adaptive Eulerian grid refinement is employed with a high-resolution Godunov differencing scheme. The adaptive mesh can be refined based on a number of criteria including gradients in physical conditions or material properties for the three phases of the landslide material (*i.e.,* water and air).

Liu et al. (2005) derived a numerical model to experimentally reproduce sliding down landslides in a wave tank. The model solves the 3D Navier-Stokes equations and is based on the Large Eddy Simulation (LES) diffusion mechanism. The volume of fluid method (VOF) is used to track the water free surface and the waves propagating alongshore (*i.e.,* induced wave runup). In the case of subaerial landslide, only the runup at the near field was considered.

Kowalik et al. (2005a,b) used a two-dimensional Navier-Stokes model (2-D NS) consistently for waves generation by rigid and deformable moving objects. The VOF method was used to track the water free surface and the shoreline evolution. The

prediction capability of tsunami generation, propagation and runup was improved by including the hydrodynamic pressure field. The model has the capability to represent complex curved boundaries within a Cartesian grid system and to deal with arbitrary transient-deformed moving boundaries. The model was verified using the analytical solutions provided in Synolakis et al. (2007) for tsunami generation and runup onto a plane beach due to 2-D landslide. The model's results were compared against shallow water models solutions to visualize differences between the two methods. Since the Navier-Stokes solution includes the vertical component of velocity/acceleration, large differences were observed when non hydrostatic effects were strong. Later, Horrillo (2006) implemented and tested the model against the aerial landslide lab-experiment described in Heinrich (1992). This experiment offers a complex wave hydrodynamic and it is of great interest to advance CFD modelers due to the presence of high nonlinearity and breaking waves.

More recently, in contrast, Schwaiger and Higman (2007) used a mesh free Lagrangian hydrocode based on the Smoothed Particle Hydrodynamics (SPH) to reduce the effects of numerical dissipation and improve tracking of the material interfaces, reproducing the 1958 Lituya Bay rockslide event.

Abadie et al. (2010) reported on the application and experimental validation of a multiple fluid Navier-Stokes model (THETIS) for wave generated by idealized slide geometries or deforming slides. The model treated all computational domain regions, *i.e.,* water, air, and slide, as Newtonian fluids, (Direct Numerical Simulations). The model has validated using analytical solution and several laboratory experiments from previous studies. In this paper, they discussed that significantly for subaerial slides, the air or water flow surrounding the slide has a substantial effect on slide motion, through hydrodynamic drag forces since the entrained air bubbles take place during the sliding motion as described in Fritz et al. (2001). The model was suc-

cessfully validated for the 3-D landslide experiment described in Liu et al. (2005); Synolakis et al. (2007).

1.3.3 Conclusions

The conclusions from the literature review are summarized below:

1. Most of landslide studies were based on the Froude similarity.

2. The identified variables of the tsunami generation induced by landslides can be expressed as a function of all the involved governing parameters:

$$A = f\left(F,\ h,\ s,\ l_s,\ b,\ V_s,\ v_s,\ M_s,\ \rho_s,\ \rho_g,\ n,\ \phi,\ \alpha,\ T_s\right) \tag{1.5}$$

3. For 3-D cases, the wave propagation depends on radial distance x or r, the time t and the propagation direction θ.

4. In most physical models, the tsunami generation was governed by the slide Flude number F, relative slide thickness s/h, hill slope α, relative distance x/h or r/h and the wave propagation direction θ.

5. The wave attenuation is underestimated in 2-D models when compared with 3-D wave propagation.

6. The maximum wave heights in 3-D models are in the direction of the slide moving ($\theta = 0^{\circ}$).

7. Lateral runup along the slope from the generated tsunami could pose a hazard (close to the generation region).

8. A fully 3-D model can accurately simulate the landslide, air, water interaction during the wave generation.

9. Review of empirical formulations indicate that wave height increase as dimensionless Froude number (F), dimensionless landslide thickness (S), and specific gravity (G) increase.

10. With respect to the slope of the incline (α), all the formulations except for the one by Huber and Hager (1997) suggested that the lower the slope, the higher the wave height.

11. The landslide front slope angle (ϕ) influence was concerned only by Kamphuis and Bowering (1970) and Heller and Harger (2010). While the larger slide front angle ϕ (or $\alpha+\phi$), the larger the impact crater and the higher wave height too.

12. 3-D water bodies lateral dispersion are modeled by a squared cosine function involving the wave propagation direction θ (measured as the direction of landslide motion). See Eq. (1.2).

13. In general, granular landslides seem to generate lower waves compared with solid one as indicated by Zweifel (2004).

14. As far as the induced wave period is concerned, the dimensionless distance (x *or* r) from wave generation region strongly acts that the higher the distance, the higher the wave period, *i.e.,* wave dispersion occurs.

15. In case of 3-D impulse wave generation, the generated wave height increases with increasing the impact velocity of landslide (v_s) and the the dimensionless landslide front area (Σ).

16. Especially in the case of subaerial landslides generated water motions, it is important to distinguish a slide impact zone to decay the induced wave height

faster due to air entrainment, large turbulence production, amplitude dispersion and frequency dispersion, such as the experimental works of Fritz et al. (2001, 2003a,b), Walder et al. (2003); Hoque and Aoki (2008); Heller et al. (2008); Heller and Harger (2010), and the numerical simulations studied by Monaghan and Kos (2000), Mader and Gittings (2002) and Panizzo et al. (2005b).

1.4 Thesis Content

This thesis is divided into five chapters. Chapter are structured as follow. Chapter 1 presents a general overview of tsunami events and discusses the need for improved tsunami calculation tools for practical application of landslide generated tsunami. The first section of this chapter contains an introduction to tsunami induced by landslides and explains why tsunamis are devastating events to the social communities. Section two includes the motivation and objectives of the research presented in this thesis. Last section presents a review of relevant literature. Chapter 2 is divided into five parts and presents a background of laboratory experiments and description of numerical models for landslide generation. The experimental setup, equipment, and procedures are outlined in section two. In third section, numerical models of full three- dimensional Navier-Stokes models (3-D NS) are discussed. Section four includes a brief introduction to the TSUNAMI3D, while section five presents a brief overview of FLOW-3D. In chapter 3, the numerical modeling setup, methodology and data collection procedures are outlined. Descriptions of the setup configurations of fjord, headland and farfield coastline domains are also presented. Chapter 4 presents the numerical results and comparison between experimental data and numerical data. Conclusions and suggestions for future work are contained in Chapter 5.

2. DESCRIPTION OF NUMERICAL MODELS USED FOR LANDSLIDE GENERATION

2.1 Introduction

Most of the incompressible-Newtonian fluid flow physics can be described by Navier-Stokes equations. Various numerical schemes have been developed in the past to solve these equations. When a free surface is present, tracking the movement of the free surface becomes a complicated task, especially when the free surface experiences severe deformation, *i.e.,* during the wave breaking process. It has been common to use the Marker and Cell (MAC) method (Harlow and Welch, 1965) and the Volume of Fluid (VOF) method (Nichols et al., 1980) to track free surface motion. One of the earliest numerical models for solving the Navier-Stokes (NS) equations was developed by Harlow and Welch (1965). In this model, the NS equations were first discretized into a forward-time finite difference form. By enforcing zero divergence of velocity field at both the previous and current time steps, the pressure at the current time step was solved with an iterative method. Then the velocity information at the new time step can be obtained with the use of updated pressure.

2.2 Governing Equation

The flow of a Newtonian, incompressible fluid with free surface and density ρ in a bounded domain Ω is governed by the equation of conservation of mass

$$\nabla \cdot \mathbf{u} = 0 \tag{2.1}$$

and the equation of momentum conservation given by

$$\frac{\partial u}{\partial t} + (\mathbf{u} \cdot \nabla)\mathbf{u} = -\frac{1}{\rho}\nabla p + \nu \nabla^2 \mathbf{u} + \mathbf{g} \tag{2.2}$$

where Eq. (2.1) represents the continuity equation, while Eq. (2.2) is known as the Navier-Stokes equation; where $\mathbf{u}(\mathbf{x}, t)$ is the velocity vector at any point $\mathbf{x} = x\hat{i} + y\hat{j} + z\hat{k}$ at time t, p is the pressure, ν is the kinematic viscosity, $\mathbf{g}$ is the gravity acceleration vector. The three-dimensional (3-D) fluid flow is solved using an Eulerian frame in which fixed points

$$\mathbf{x} = x\hat{i} + y\hat{j} + z\hat{k}$$

in the domain $\Omega(t)$ are described in a Cartesian system of coordinates (Fig. 2.1).

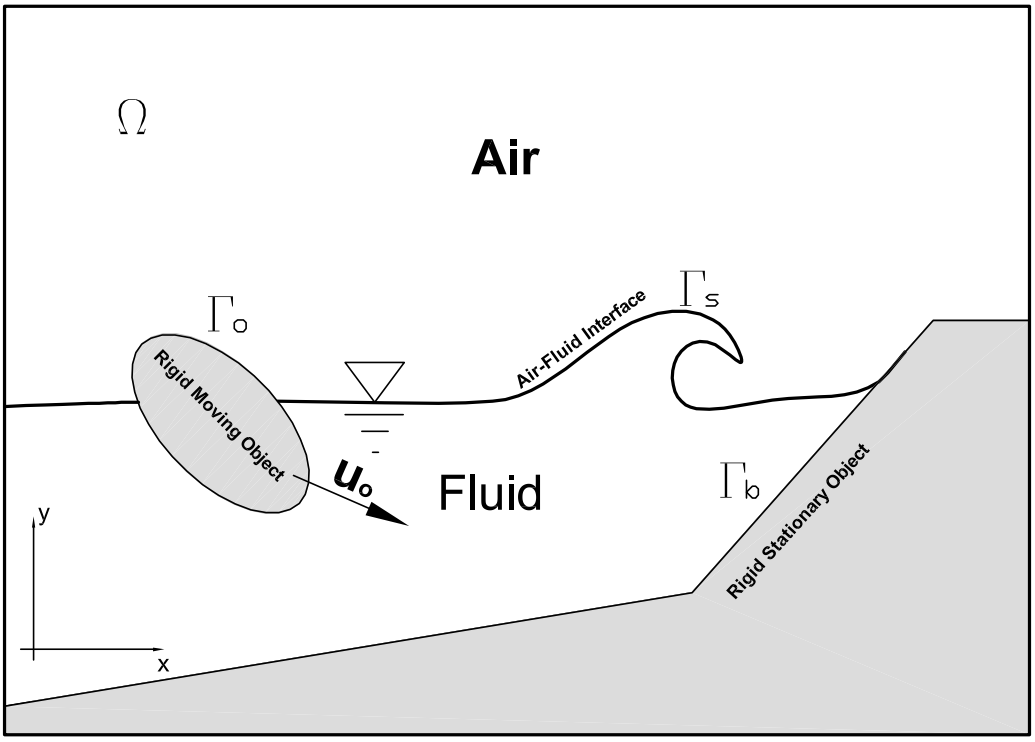

Figure 2.1: A typical computational domain with moving and stationary objects. Courtesy Dr. Juan J. Horrillo, Texas A&M at Galveston.

2.2.1 Discretization of the Governing Equations

Numerical solutions require the domain to be discretized and the governing equations to be reduced to their finite difference equivalents. Fig. 2.2a shows the grid employed for the discretization. In a variable staggered grid, quantities such as p and VOF function F are defined at the center of the cell, while the horizontal component of velocity is displaced half a grid to the right from the center and the vertical component is displaced half a grid up from the center, see Section 2.2.4. For application to shallow coastal waters and wave generation areas, high spatial resolution is rather imperative so that the shorter spatial-time scale typical of the process in these regions can be resolved. A staggered slowly variable grid is better suited to these applications. The objective is to solve for the unknown variables u, v, p and F as a function of time, starting from a specified set of initial static-conditions (*i.e.,* tsunami source waves) or dynamic-conditions (*i.e.,* landslide, seabottom uplift, rock impact, etc.) with an appropriate boundary condition treated according to the model requirements.

The governing equations are solved using a finite difference method (FDM), which are basically the same principles used in the marker and cell (MAC) method by Harlow and Welch (1965). They introduced a finite difference solution scheme for solution of the velocity field in which the staggering of pressures, densities (VOF function) and velocities results in second order central difference. This configuration also implies offset of the momentum control volume centered at the cell side, and cell volume centered at the cell center.

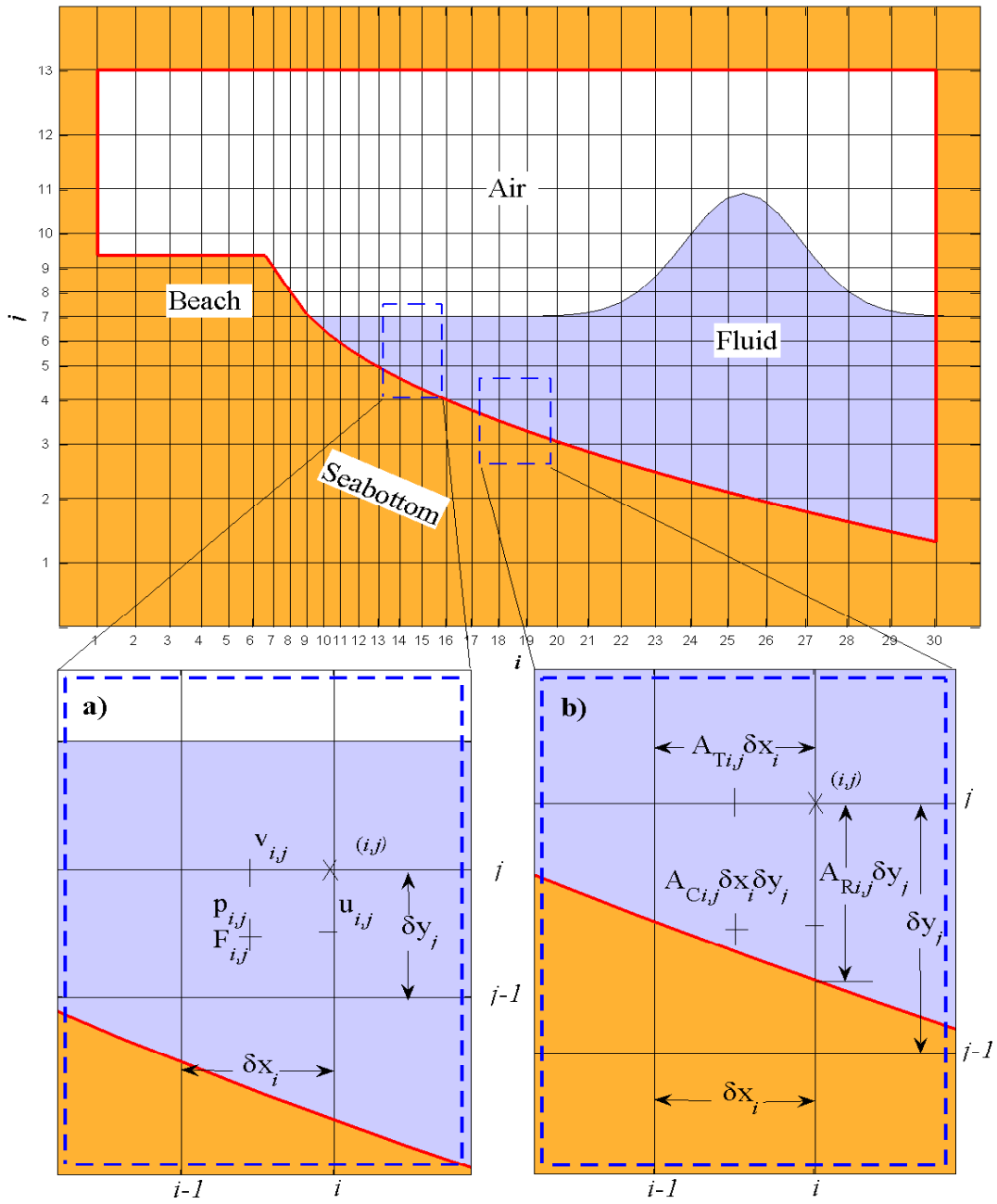

Figure 2.2: A typical tsunami computational domain: (a) Location of variables in a computational cell. The horizontal ($u_{i,j}$) and vertical ($v_{i,j}$) velocity components are located at the right cell face and top cell faces, respectively. The pressure $p_{i,j}$ and VOF function $F_{i,j}$ are located at the cell center; (b) Volume and side cell apertures. Courtesy Dr. Juan J. Horrillo, Texas A&M at Galveston.

2.2.2 Free Surface Equation

In case of the most fluid flow problems including impulsive waves or tsunamis, parts of computational domain are filled with fluid and a sharp interface or free surface which separates the fluid from the air. The most practical method is the tracking of the free surface using the Eulerian description. The basic governing equation is

$$\frac{\partial \rho}{\partial t} + \mathbf{u} \cdot \nabla \rho = 0 \tag{2.3}$$

which is referred to as the transport equation. The density $\rho(\mathbf{x}, t)$ can be continuous or a step function. By tracking the change of ρ, it is possible to identify the location of the free surface. Directly using the numerical version of Eq. (2.3), one may end up with excessive numerical diffusion, so other approaches have been used for such a purpose. Nichols et al. (1980) developed the VOF method to track the free surface.

The principle of the VOF method is simple. By using the transport equation and assuming that density is everywhere constant ($\rho = \rho_o$) in the flow domain and zero ($\rho = 0$) in the air domain, it is possible to normalize the transport equation by ρ_o. Defining $F = \rho/\rho_o$ as the fractional volume of fluid function (VOF function), the free surface can be described by a scalar field $F(\mathbf{x}, t)$ which satisfies the the transport or conservation equation as

$$\frac{dF}{dt} = \frac{\partial F}{\partial t} + \mathbf{u} \cdot \nabla F = 0 \tag{2.4}$$

in which F propagates with the fluid velocity u. $F(\mathbf{x}, t)$ at time $t = 0$ is given and the fluid density does not change in time. F is a step function, where $F = 1$ in elements containing fluid and $F = 0$ in elements containing air. In free surface elements, the value of F ranges between 0 and 1. Given the velocity field, one may update F using a special treatment of Eq. (2.4). Therefore, by tracking the VOF function F, one

can identify the free surface elements at any time step.

2.2.3 Boundary Condition

Tsunami sources are specified through the initial and boundary conditions. Boundary conditions are needed at the free surface and at the stationary or moving boundaries. The boundary conditions will introduce the dynamics and determine the nature of the solution.

2.2.3.1 Stationary and Moving Boundary Condition

At the solid boundary of a stationary or moving object, it is common to use Dirichlet (no-slip) and Neumann (free-slip) boundary conditions (Morse and Feshbach, 1953). For instance, for the solid boundary, the fluid velocity is equal to the boundary velocity $\mathbf{u_o} = (u_o\ \hat{i} + v_o\ \hat{j})$, thus

$$\mathbf{u} = \mathbf{u}_o, \qquad \text{on} \ \ \Gamma_b \text{ or } \Gamma_o, \tag{2.5}$$

see Fig. 2.1. For stationary boundaries, $\mathbf{u} = \mathbf{u}_o = 0$ on Γ_b, as seen in Fig. 2.1. This states that the boundary is impermeable and the fluid sticks to the wall due to the viscous effect, this is commonly known as no-slip boundary condition. However, in some situations a free-slip boundary condition as

$$u_{norm} = 0 \ \ \text{and} \ \ \frac{\partial u_{tang}}{\partial \mathbf{n_{orm}}} = 0, \qquad \text{on} \ \ \Gamma_b \tag{2.6}$$

is prescribed to a stationary object, meaning that shear stresses are neglected at the solid boundary. Here, $u_{norm} = \mathbf{n_{orm}} \cdot \mathbf{u}$ and $u_{tang} = \mathbf{t_{ang}} \cdot \mathbf{u}$ denote the normal and tangential velocity at the stationary solid boundary, see Fig. 2.3. $\mathbf{t_{ang}}$ and $\mathbf{n_{orm}}$ are the unit tangential and unit normal vectors, respectively.

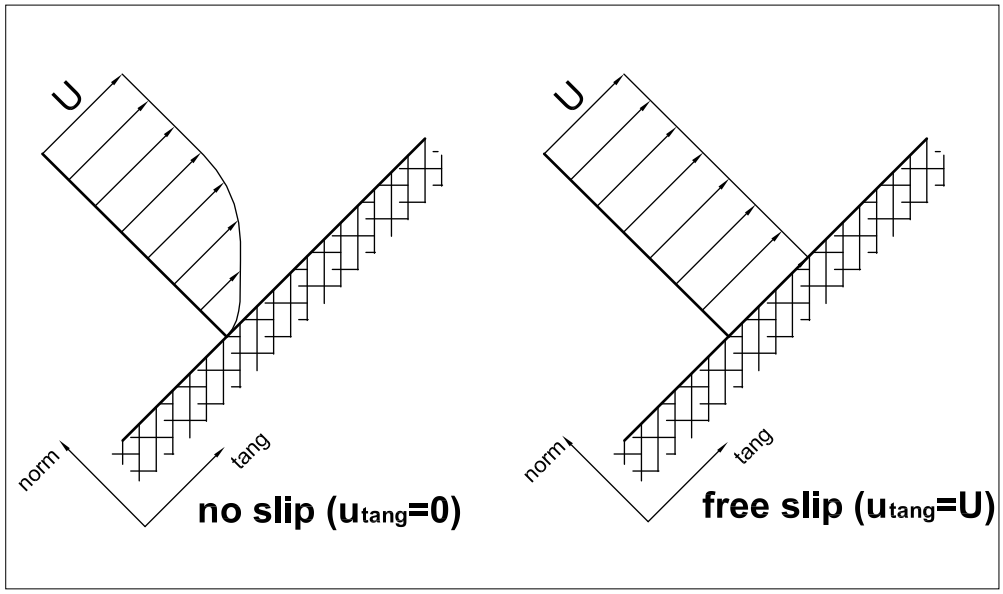

Figure 2.3: Velocity profile and boundary condition near a stationary object. Courtesy Dr. Juan J. Horrillo, Texas A&M at Galveston.

On the other hand, along a moving boundary Γ_o, the immediate fluid particle must have the same velocity as that of the moving boundary. In general, along any solid boundary (Γ_b, Γ_o) the fluid velocity must be the same as that of the boundary itself. The most important boundary condition will be at the free surface, Γ_s. In fact, this is where the dynamics of the fluid enters and it is often the most difficult to implement.

2.2.3.2 Free Surface Boundary Condition

The distinctive behavior of water waves results from the physical boundary conditions at the interface between air and water. In numerical calculations the position of the water-air interface or sea surface is known only at the initial stage. Along the free surface, both dynamic and kinematic boundary conditions are needed. The

dynamic boundary condition describes the stresses acting on the free surface, and the kinematic boundary condition describes the movement of the free surface. For the dynamic boundary condition, the normal and tangential stress components must be continuous and can be expressed as

$$-p + 2\mu \frac{\partial u_{norm}}{\partial \mathbf{n_{orm}}} = -p_o + \sigma\kappa, \tag{2.7}$$

and

$$\mu \left(\frac{\partial u_{norm}}{\partial \mathbf{t_{ang}}} + \frac{\partial u_{tang}}{\partial \mathbf{n_{orm}}} \right) = 0 \quad on \;\; \Gamma_s \tag{2.8}$$

(Kothe et al., 1991), where *norm* and *tang* denote the outward normal and the tangential directions, respectively. p_o is the air pressure, σ is the surface tension and κ denotes the curvature of the free surface. The dynamic boundary condition usually includes the approximation that the air pressure is constant or zero. This approximation serves to decouple the motion of the air from that of the water. In tsunami or gravity wave calculations, the surface tension term can be neglected since gravitational and inertial forces dominate. Also, the viscous effects are neglected at the free surface (second term on the left-hand side of Eq. 2.7), since it is small compared with the other terms due to the small value of the molecular viscosity. In summary, the resultant equation for the dynamic of the water is solved without considering the motion of the air, surface tension and viscous effects. Doing so, Eq. (2.7) reduces to $p = p_o$.

Besides the dynamic condition, the kinematic boundary condition describing the free surface motion is also needed. Although the application of the kinematic boundary condition is standard following a Lagrangian or Eulerian approach, one may derive various forms of kinematic boundary conditions, which serve as the basis of

different tracking techniques. Appropriate free surface boundary condition must be applied using any of those techniques on the air-water interface in conjunction with stationary and moving objects to satisfy the balancing forces. The position of the free surface boundary is known only at the initial stage, $t = 0$, thus the free surface position at later times has to be determined, and it is critical for the solution of the entire system and subsequent free surface locations.

From a Lagrangian system of coordinates, the transport equation (Eq. 2.4) describing the motion of a particle resting on the free surface can be written as

$$\mathbf{u} = \frac{d\mathbf{X}(t)}{dt} \tag{2.9}$$

where $\mathbf{X}$ is the position vector of a fluid particle on the free surface at time t. The above equation implies that the fluid particle moves in accordance with the ambient flow field. If one tracks particles that are originally on the free surface based on Eq. (2.9), these particles will remain on the free surface unless the free surface breaks and reconnects. Note that this is a general equation which can be applied not only on the free surface but also to the entire fluid.

The Eulerian approach for tracking the free surface is to update the free surface location based on conservation or transport Eq. (2.4). F is a scalar function carrying the material information. The equation states that $F(\mathbf{x}, t)$ propagates with the fluid velocity without changing the material property. For instance, if $F(\mathbf{x}, t) = \rho$ then this density can be transported conserving its property (incompressible fluid).

Accurately tracking the free surface movement is important for accurately predicting wave evolution, therefore an appropriate boundary condition must be applied on the interface to satisfy the balancing forces.

2.2.4 Location of Variable and Apertures

Discrete values of the time dependent variables, including the fractional volume of fluid F used in the VOF technique, are located at cell positions shown in Fig. 2.2a. Velocity components u and v are located in the cell right face and top face respectively. Discrete values of pressure p and VOF function F are located at the cell center.

As seen from Fig. 2.2, cell variables are referenced with respect to the cell right-upper corner or indexes intersection, e.g., $(i,\ j)$. This particular method for variable location differs from those commonly found in the literature, where half indexes are used instead. This system has been adopted in this study since it is more consistent with algorithm construction.

Solution of the system is obtained using the central-variable configuration by means of the staggered grid scheme. Central configuration facilitates the calculation of momentum and fluxes amongst cells, and the resulting numerical algorithms are particularly simple and computationally efficient. However, while using the staggered grids, there is limitation of rectangular elements: the treatment of boundary condition when object or surface interfaces cut a computational cell. Therefore, to eliminate the discrete steps and allow a better geometric representation of curved object surfaces, a technique is used. This technique keeps the rectangular elements, but supplements them with a function that defines the obstacle-cutting in the elements interior. Such a technique is called Fractional Area Volume Obstacle Representation (FAVOR), Nichols et al. (1980). With the FAVOR technique, the geometry of a stationary or moving object can take any arbitrary shape. Object geometry is then defined within the grid by computing the fractional face areas and fractional volume of each element that is blocked by the object, see Fig. 2.2b. Open fractional cell face

areas (right and top cell sides) and volume for the fluid to flow, $A_{T_{i,j}}$, $A_{R_{i,j}}$ and $A_{C_{i,j}}$, are referred to herein as apertures. They are calculated based on the complement of the fractional blocked face areas and volume, thus, $A_{T_{i,j}} = 1 - B_{T_{i,j}}$, $A_{R_{i,j}} = 1 - B_{R_{i,j}}$ and $A_{C_{i,j}} = 1 - B_{C_{i,j}}$, respectively. Here $B_{T_{i,j}}$, $B_{R_{i,j}}$ and $B_{C_{i,j}}$ represent the fraction of cell face areas and volume that are blocked for the object. Thus, this technique retains the simplicity of rectangular elements, while representing complex geometric shapes at a level consistent with the use of averaged flow quantities within each volume element, and the grid and object geometries can be generated and modified with very little time or effort.

2.2.5 Cell Labeling

Having the cell face areas and volume apertures calculated from the object geometry, the cells can be categorized as fluid flow cell ($A_C > 0$) and object cell ($A_C = 0$), see Fig. 2.4a. Fluid flow cells are open for fluid to fill them. They are filled by the initial condition or filled or emptied by the established fluid forcing. A fluid flow cell has to be distinguished from cells in air, immersed in the fluid or between the air and fluid. This is done by the volume of fluid function F that identifies cells that contain fluid with density ρ_{fluid}. Cells with zero F values are empty (E) or contain material of density $\rho_{air} = 0$. A cell with free surface or air-fluid interface (S) at, *e.g.,* $(i,\ j)$, is defined as a cell containing a nonzero value of F and having at least one neighboring cell $(i \pm 1,\ j)$ or $(i,\ j \pm 1)$ that contains a zero value of F (empty cell). Cells with nonzero F values and no empty neighbors are treated as full (F) cells with ρ_{fluid}, see Figs. 2.4b and c. In summary, fluid flow cells can be empty (E), full (F) or surface (S) cells. Object cells (O) have one distinction as boundary object cells (B), when the cell has at least one neighboring fluid flow cell, *i.e.,* (E), (F) or (S), see Fig. 2.4c. In practical tsunami applications, often the influence of the air flow is

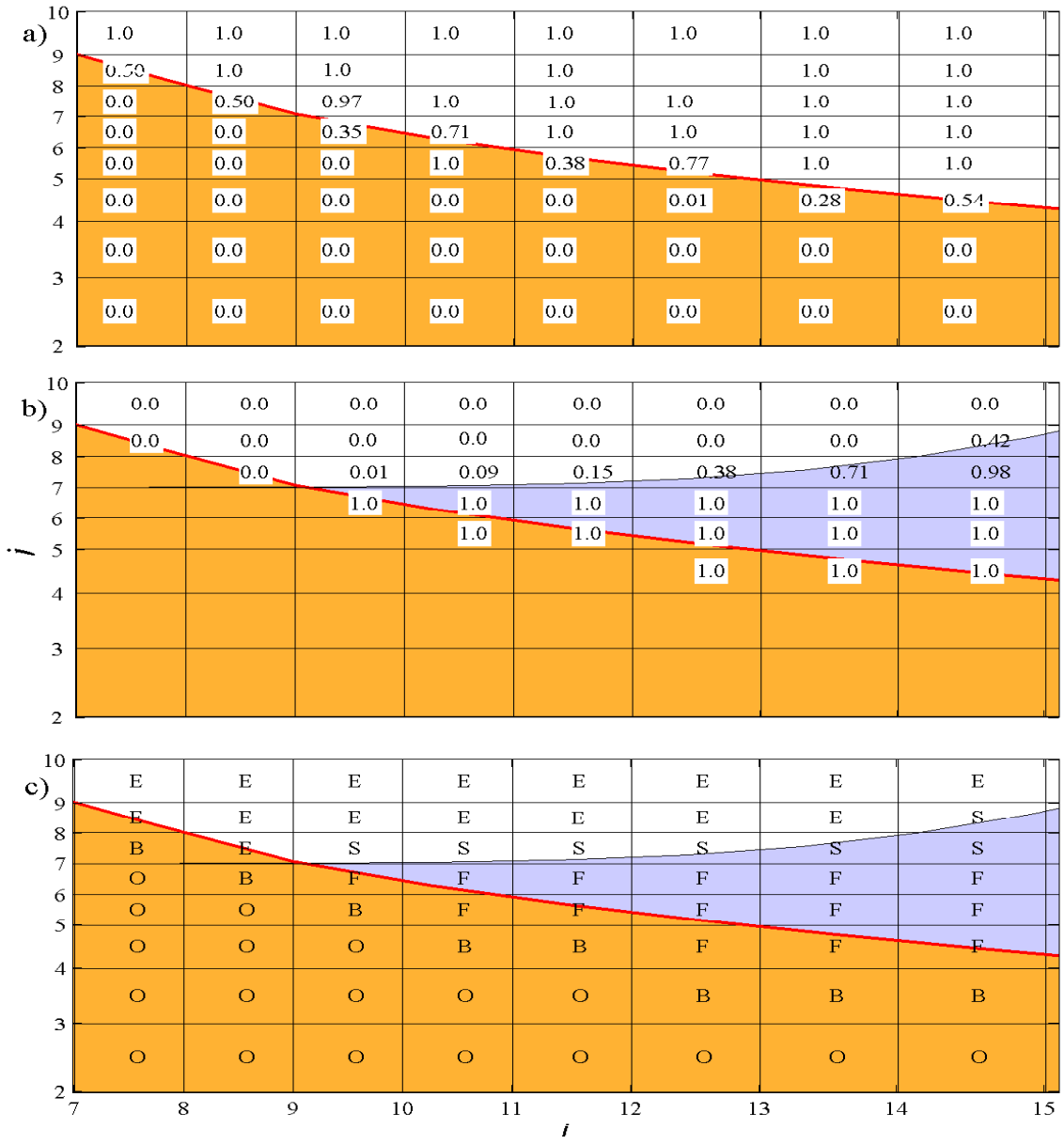

Figure 2.4: Fluid flow cells, volume of fluid function and cell labeling: (a) Fluid flow cells (cell volume aperture $A_C > 0$) and object cells (cell volume aperture $A_C = 0$); (b) Volume of fluid function values ($0 \leq F \leq 1$); (c) Cell labeling: (E)mpty, fluid flow cell without fluid ($A_C > 0$, $F = 0$): (S)urface, fluid flow cell partially or completely filled by fluid and neighboring at least one empty cell: (F)ull, fluid flow cell completely or partially filled by fluid and no empty neighbors: (O)bject, cell completely occupied by the object: (B)oundary, object cell neighboring at least one fluid flow cell ((E), (F) or (S)). Courtesy Dr. Juan J. Horrillo, Texas A&M at Galveston.

assumed to be irrelevant to the wave propagation; thus, calculations are avoided in empty (E) cells. The cell labeling facilitates the application of boundary conditions and improves computational performance, since calculations are often excluded in empty and object cells. The cell labeling is needed in the application of boundary conditions as well for instance, the pressure boundary conditions are required in surface (S) cells, velocity boundary conditions are required in surface-empty (S)-(E) cell faces and (E)-(E) cell faces, *e.g.,* for the tangential boundary condition for (S)-(S) velocities.

2.2.6 Stability Conditions

One of the main goals in fluid dynamic computation is to achieve an acceptable numerical reproduction of a physical phenomena. Therefore, there are differences between the approximated solution and the true physical solution. Discretization errors are introduced by the spatial and temporal discretization used in the computational domain. They can be easily reduced by refining the computational grid and reducing the time step. Successive refinement of grid size and time step is commonly practiced in numerical simulation to find efficient grid-independent domains and stable solutions. Discretization errors are the most flexible to control by model users. The discretization errors are mostly related to the advection terms, so the analysis is focused on the advection terms numerical stability. Since the advection terms are evaluated explicitly, the time step T adopted must be smaller than a certain critical value to prevent instability. Firstly, a parcel of fluid or moving object cannot travel more than one cell width per time step. The advection of the F function (Section 2.2.2), as well as the momentum advection discussed previously in Section 2.2.1, is approximated explicitly in time. Typically, T is chosen to be some fairly small fraction of the minimum value, so the constraint is imposed by means of the Courant-

Friedrichs-Lewy (CFL) number, N_{CFL}. This constraint must be enforced along both coordinate directions, so the transport time step limit T, is taken as the minimum of the transport time step limits of the x-direction and y-direction, thus

$$T < N_{CFL} \min \left[\frac{(\delta x_i)}{|u_{i,j}|}, \frac{(\delta y_j)}{|v_{i,j}|} \right]. \tag{2.10}$$

The multiplier N_{CFL} should be less than 1.0 in theory, or more conservatively, less than 1/2 in practice. A value of $N_{CFL} = 0.33$ is recommended for tsunami calculations. Secondly, the frictional term is evaluated using old time t^m velocity field. This explicit treatment is therefore subjected to a linear stability time step constraint, which is evaluated conservatively under the premise that the momentum must not diffuse more than one cell in one time step, thus

$$T < \frac{1}{2\nu} \min \left[\frac{(\delta x_i)^2 (\delta y_j)^2}{(\delta x_i)^2 + (\delta y_j)^2} \right]. \tag{2.11}$$

These stability conditions are only approximate, since they are based on the linear von Neumann analysis, which does not include the simultaneous effect of the pressure gradient in the momentum equation. If the advection flux exceeds more than 1/3 of the cell volume, the time step T is reduced automatically and all calculations are restarted with the reduced T.

2.3 Methodology Used for Two Fluid Simulations

Both 3D-NS models solve the full Navier-Stokes equations and the continuity equation for incompressible flow along with the Volume of Fluid Method(VOF) (Hirt and Nichols, 1981) to track the fluid free surface motion. A brief description of the models follows:

TSUNAMI3D code solves transient fluid flow with free surface boundaries based on the concept of the fractional volume of fluid (VOF), and it uses a sharp interface approach using a simplified general eddy viscous formulation described by two phase fluid, *i.e.,* water and mud with Direct Numerical Simulation (DNS) approach. In the commercial package, FLOW-3D, the sediment scour model uses a bulk approximation of a conservation of mass and advection/diffusion scheme to predict the transport of sediment. The fluid motion is achieved by density/pressure gradient and particle drag coefficient as a results of the shear stress of the water phase to the mud particles.

2.3.1 TSUNAMI3D

TSUNAMI3D has been developed by the University of Alaska Fairbanks (UAF) and Texas A&M University at Galveston (TAMUG) and it is dubbed TSUNAMI3D for **T**sunami **S**olution **U**sing **N**avier-Stokes **A**lgorithm with **M**ultiple **I**nterfaces. This model solves transient fluid flow with free surface boundaries based on the concept of the fractional volume of fluid; the model uses an Eulerian mesh of rectangular cells having variable sizes. The fluid equations solved are the finite difference approximation of the Navier-Stokes and the continuity equations. The basic mode of operation is for single fluid calculation having multiple free surfaces. TSUNAMI3D model can also be used for calculations involving two fluids separated by a sharp or non-sharp interface, *i.e.*, water and mud. The models is suitable for complex tsunami wave generation due to the capabilities: (a) moving or deformable objects,

(b) subaerial/submarine landslide considering simplified soil rheology, and (c) complex vertical or lateral bottom deformation.

In TSUNAMI3D, the governing equations to describe the flow of two incompressible Newtonian fluids (*e.g.,* water and mud) on domain $\Omega(t)$ are the mass conservation equation as expressed as Eq. (2.1)

$$\frac{\partial u}{\partial x} + \frac{\partial v}{\partial y} + \frac{\partial w}{\partial z} = 0 \tag{2.12}$$

and the conservative equation of momentum given by Eq. (2.2) becomes:

1. For the first layer (water phase)

For x-direction,

$$\begin{aligned} &\frac{\partial u}{\partial t} + \frac{\partial uu}{\partial x} + \frac{\partial uv}{\partial y} + \frac{\partial uw}{\partial z} \\ &\qquad = -g\frac{\partial \eta_1}{\partial x} - \frac{1}{\rho_1}\frac{\partial q}{\partial x} + \frac{\partial}{\partial x}\left[\frac{\mu_1}{\rho_1}\left(2\frac{\partial u}{\partial x}\right)\right] \\ &\qquad + \frac{\partial}{\partial y}\left[\frac{\mu_1}{\rho_1}\left(\frac{\partial u}{\partial y} + \frac{\partial v}{\partial x}\right)\right] + \frac{\partial}{\partial z}\left[\frac{\mu_1}{\rho_1}\left(\frac{\partial u}{\partial z} + \frac{\partial w}{\partial x}\right)\right] \end{aligned} \tag{2.13}$$

For y-direction,

$$\begin{aligned} &\frac{\partial v}{\partial t} + \frac{\partial uv}{\partial x} + \frac{\partial vv}{\partial y} + \frac{\partial vw}{\partial z} \\ &\qquad = -g\frac{\partial \eta_1}{\partial y} - \frac{1}{\rho_1}\frac{\partial q}{\partial y} + \frac{\partial}{\partial x}\left[\frac{\mu_1}{\rho_1}\left(\frac{\partial v}{\partial x} + \frac{\partial u}{\partial y}\right)\right] \\ &\qquad + \frac{\partial}{\partial y}\left[\frac{\mu_1}{\rho_1}\left(2\frac{\partial v}{\partial y}\right)\right] + \frac{\partial}{\partial z}\left[\frac{\mu_1}{\rho_1}\left(\frac{\partial v}{\partial z} + \frac{\partial w}{\partial y}\right)\right] \end{aligned} \tag{2.14}$$

For z-direction,

$$\begin{aligned}\frac{\partial w}{\partial t}+\frac{\partial uw}{\partial x}+\frac{\partial vw}{\partial y}+\frac{\partial ww}{\partial z}&\\ =&\frac{1}{\rho_1}\frac{\partial q}{\partial z}+\frac{\partial}{\partial x}\left[\frac{\mu_1}{\rho_1}\left(\frac{\partial w}{\partial x}+\frac{\partial u}{\partial z}\right)\right]\\ &+\frac{\partial}{\partial y}\left[\frac{\mu_1}{\rho_1}\left(\frac{\partial w}{\partial y}+\frac{\partial v}{\partial z}\right)\right]+\frac{\partial}{\partial z}\left[\frac{\mu_1}{\rho_1}\left(2\frac{\partial w}{\partial z}\right)\right]\end{aligned} \tag{2.15}$$

where, $u=(x,y,z,t)$, $v(x,y,z,t)$ and $w(x,y,z,t)$ are the velocity components along the coordinate axes of the fluid at any point

$$\mathbf{x}=x\hat{i}+y\hat{j}+z\hat{k}$$

at time t. Subscript 1 represent physical parameters corresponding to the water phase. Therefore, $\eta_1(x,y,z)$ is the water surface elevation measured from a vertical datum, ρ_1 is the density of the fluid, q is the non-hydrostatic pressure, μ_1/ρ_1 can be related to the water eddy viscosity and g is the acceleration due to gravity. The total pressure, $p=p_{hyd}+q$, has been divided into a hydrostatic pressure $p_{hyd}=\rho_1 g(\eta_1-z)$ and a non-hydrostatic (dynamic) pressure q such that $\partial p_{hyd}/\partial z=-\rho_1 g$. Here z is the elevation measured from a vertical datum to the cell center as shown in Fig. 2.2.

2. For the second layer (mud phase)

For x-direction,

$$\begin{aligned}\frac{\partial u}{\partial t}+\frac{\partial uu}{\partial x}+\frac{\partial uv}{\partial y}+\frac{\partial uw}{\partial z}&\\ =&-g\left(\gamma\frac{\partial \eta_1}{\partial x}+(1-\gamma)\frac{\partial \eta_2}{\partial x}\right)-\frac{1}{\rho_2}\frac{\partial q}{\partial x}+\frac{\partial}{\partial x}\left[\frac{\mu_2}{\rho_2}\left(2\frac{\partial u}{\partial x}\right)\right]\\ &+\frac{\partial}{\partial y}\left[\frac{\mu_2}{\rho_2}\left(\frac{\partial u}{\partial y}+\frac{\partial v}{\partial x}\right)\right]+\frac{\partial}{\partial z}\left[\frac{\mu_2}{\rho_2}\left(\frac{\partial u}{\partial z}+\frac{\partial w}{\partial x}\right)\right]\end{aligned} \tag{2.16}$$

For y-direction,

$$\frac{\partial v}{\partial t}+\frac{\partial uv}{\partial x}+\frac{\partial vv}{\partial y}+\frac{\partial vw}{\partial z} \\ =-g\left(\gamma\frac{\partial \eta_1}{\partial y}+(1-\gamma)\frac{\partial \eta_2}{\partial y}\right)-\frac{1}{\rho_2}\frac{\partial q}{\partial y}+\frac{\partial}{\partial x}\left[\frac{\mu_2}{\rho_2}\left(\frac{\partial v}{\partial x}+\frac{\partial u}{\partial y}\right)\right] \\ +\frac{\partial}{\partial y}\left[\frac{\mu_2}{\rho_2}\left(2\frac{\partial v}{\partial y}\right)\right]+\frac{\partial}{\partial z}\left[\frac{\mu_2}{\rho_2}\left(\frac{\partial v}{\partial z}+\frac{\partial w}{\partial y}\right)\right] \tag{2.17}$$

For z-direction,

$$\frac{\partial w}{\partial t}+\frac{\partial uw}{\partial x}+\frac{\partial vw}{\partial y}+\frac{\partial ww}{\partial z} \\ =-\frac{1}{\rho_2}\frac{\partial q}{\partial z}+\frac{\partial}{\partial x}\left[\frac{\mu_2}{\rho_2}\left(\frac{\partial w}{\partial x}+\frac{\partial u}{\partial z}\right)\right] \\ +\frac{\partial}{\partial y}\left[\frac{\mu_2}{\rho_2}\left(\frac{\partial w}{\partial y}+\frac{\partial v}{\partial z}\right)\right]+\frac{\partial}{\partial z}\left[\frac{\mu_2}{\rho_2}\left(2\frac{\partial w}{\partial z}\right)\right] \tag{2.18}$$

where subscript 2 represents physical parameters corresponding to the mud phase. $\eta_2(x,y,t)$ is the mud-surface elevation measured from a vertical datum, ρ_2 is the mud density, γ is the fluid-mud density ratio given by ρ_1/ρ_2. The total pressure $p = p_{hyd}+q$ has been divided into the hydrostatic pressure $p_{hyd} = g[\rho_1(\eta_1-\eta_2)+\rho_2(\eta_2-z)]$ and the dynamic pressure q. In this study or for the selected laboratory experimental case, the mud is considered as a Newtonian fluid. However, the kinematic viscosity, μ_2/ρ_2, can be related to a constitutive model for mud rheology (non-Newtonian fluid). The velocities u, v and w associated with a computational cell is located at the right, back and the top cell faces respectively. The non-hydrostatic pressure $q(x,y,z,t)$ and the hydrostatic are located at the cell center as indicated in Fig 2.2. The simplified VOF method is used based on the donor-acceptor algorithm (Hirt and Nichols, 1981), featuring a scalar function $F_{1,2}(x,y,z,t)$ to define the water or

mud region in space and time. The F function accounts for the fractional volume of water or mud contained in the cell (fluid or/and mud concentration). A unit value for F corresponds to a fluid cell totally filled with water or mud, while a value of zero indicates an empty cell. Therefore, cells with F value between $(0-1)$ indicate a surface or a water-mud interface cell. The equation describing the F function is given by

$$\frac{dF_{1,2}}{dt} = \frac{\partial F_{1,2}}{\partial t} + \frac{\partial uF_{1,2}}{\partial x} + \frac{\partial vF_{1,2}}{\partial y} + \frac{\partial wF_{1,2}}{\partial z} = 0 \tag{2.19}$$

which states that $F_{1,2}$ propagates with the fluid velocity $\mathbf{u} = u\hat{i} + v\hat{j} + w\hat{k}$. Physical properties in each cell element, *i.e.,* the density and eddy viscosity, can be weighted in term of the $F_{1,2}(x, y, z, t)$ function. For example, a general expression for density is determined by the following equation and condition:

$$\rho(x, y, z, t) = \rho_1(F_1 - F_2) + \rho_2 F_2 \quad ; \quad F_1 >= F_2. \tag{2.20}$$

Eq. (2.20) indicates that advection of the second fluid (mud) requires the existence of the first fluid (water) in the cell such that $F_1 >= F_2$ (saturated condition). For instance, an insulated mud parcel to the atmosphere/void (subaerial landslide case) the value of F_1 always equals F_2 in the control volume cell ($F_2 = F_1$). This technique greatly simplifies calculations of both free surfaces, since the advection algorithm for the second fluid (mud) is an external procedure that is completed once the advection of the first fluid (water) is done.

The scalar function F and the non-hydrostatic pressure q are located at the cell center, as seen in Fig. 2.2. Eq. (2.19) can only be solved in the water and mud phases. The water and mud surface elevations $\eta_{1,2}(x, y, t)$ are a mere byproduct of $F_{1,2}$, and they are calculated by locating the water/void or mud/water interfaces along the

water/mud column at each (x, y) location in time. This implies that breaking waves are not allowed, since just one value of η_1 and η_2 are kept for each (x, y) location. This assertion is valid for cells with large distortion ratio (horizontal/vertical scale) much greater than 2 which is a common in mesh generation for practical tsunami calculations.

For the discretization of the computational domain, the model uses an Eulerian mesh of rectangular cells having variable sizes. The governing equations are solved by using the standard volume difference scheme starting with field variables such as $\mathbf{u}$, q and F are known at time $t = 0$. Notice that η is a function of F and is known once F is determined. All variables are treated explicitly with the exception of the non-hydrostatic pressure field q, which is implicitly determined. The governing equations are solved by discretization field variables spatially and temporally in the domain to obtain new field variable at any required time. Nonlinear terms are approximated using up-wind and down-wind approach up to the third order. The hydrodynamic pressure field q is calculated through the Poisson's equation by using the incomplete Choleski conjugated gradient method to solve the resulting linear system of equations.

The scale of turbulence is mainly accomplished by using a simplified general eddy viscous formulation described by two phase fluid, water and mud, referred as Direct Numerical Simulation (DNS). The DNS approximations is presumably correct in case the computational domain is relatively well resolved.

As far as the simplified general eddy viscous formulation indicated previously in the momentum equation is considered, the friction term can be tuned up for internal friction within the water body by means of the water eddy viscosity. For instance, in practical tsunami calculation, a value of water eddy viscosity μ_1/ρ_1 typically ranges between 10^{-6} m^2/sec to 10^{-5} m^2/sec. On the other hand for mud, a typical value

for μ_2/ρ_2 ranges between $10^1\ m^2/sec$ to $10^3\ m^2/sec$. At the water-mud interfaces the expression and condition indicated for density expression in Eq. (2.20). The eddy viscosity expression for water-mud interface cells reads

$$\frac{\mu}{\rho}(x,y,z,t) = \frac{\mu_1}{\rho_1}(F_1 - F_2) + \frac{\mu_2}{\rho_2}F_2. \tag{2.21}$$

For well resolved domain (fine resolution), additional friction mechanisms often are consider into the model, for instance, the no-slip condition. The no-slip condition enforced a linear decay of the velocity at all computational cells in contact with the sea-bottom or walls, *i.e.,* $\partial u/\partial z \neq 0$. Other mechanism implemented to mimic further the bottom friction is by means of an exponential function which increases the fluid eddy viscosity to one or several order of magnitude at computational fluid cells located at some short distance from the sea-bottom or walls.

2.3.2 FLOW-3D

FLOW-3D (Flow Science, Inc., Santa Fe, N. M. 2009) is a general purpose computational fluid dynamic simulation software package based on the algorithms for simulating fluid flow that were developed at Los Alamos National Laboratory in the 1960s and 1970s (Hirt and Nichols, 1981; Harlow and Welch, 1965; Welch et al., 1994). Most of the terms in the momentum equations are evaluated using the current time-level values of the local variables in an explicit fashion, though a number of implicit options are available. The pressure and velocity are coupled implicitly through the time-advanced pressures in the momentum equations and the time-advanced velocities in the continuity equation. It employs an iterative method to solve these semi-implicit equations using relaxation techniques. The sediment scour model, which predicts the behavior of suspended sediments, is used in the simulations for the deformable slide source. Some of the features include:

1. Numerical Modeling and Meshing(Geometry) Options

   (a) Volume of Fluid (VOF) method for fluid interfaces with sharp and diffuse interface tracking

   (b) Implicit & explicit numerical methods and GMRES or SOR implementation, point and line relaxation pressure solvers

   (c) Finite element meshes for solids and Structured finite difference/control volume meshes with Cartesian or cylindrical coordinates

   (d) Import CAD data as inputing from Stereo lithography (STL) file

   (e) Multi-Block griding with nested & linked meshes

   (f) Fractional area/volumes (FAVOR) for efficient and accurate geometry definition

   (g) Inviscid, viscous lamina & turbulent flow with two phase flows as one or two incompressible fluids

   (h) Two-component mixtures (drift-flux model)

   (i) Turbulence models - RNG model, Two-equation $k - \varepsilon$ model and Large eddy simulation

2. Physical Modeling Options

   (a) Fluid structure interaction

   (b) Sediment scour deposition & bedload transport

   (c) Surface tension, cavitation and air entrainment

   (d) Molecular & turbulent diffusion - Monte-Carlo diffusion

3. Maritime Applications

(a) Fluid structure interaction model such as simulating moored ships using string & Ropes capability, tug boats, offshore platforms and offloading (FPSO) system and rising .

- General Moving Object (GMO) model - 6 degrees of Freedom with rotating/spinning objects.

(b) Hull and Vessel Design - Seakeeping as a hull design, sloshing for liquid cargo and propellant motion in fuel tanks

(c) Coastal erosion and Shoreline structures -

- Multi-Sediment Scour & Bed Load Transport model

(d) Wave Modeling - Modeling wave propagation

- Wave generator model based on Fourier series - Non-linear periodic and solitary surface waves

(e) Wave Impact or damping - load predictions on marine structures

2.3.2.1 Sediment Scour Model

The sediment scour method uses two concentration fields: (a) the suspended mud which is transported by advection along with the fluid and (b) the packed mud which does not move along with the fluid. The model consists of two basic components: drifting and lifting. The drifting component acts on mud particles that are suspended in the flow; gravity (along with other body forces) causes the settling of the mud sediment. Lifting takes place only at the interface between the packed sediment and fluid and occurs where the local shear stress imposed by the liquid exceeds a critical value on the bed interface. In conjunction with the drifting and lifting models, a large drag coefficient is used to mimic the solid-like behavior of the mud slide in regions where its concentration exceeds a cohesive solid fraction. This solid-like behavior

is predicted by imposing a linear drag term to the momentum equation, as in flow through porous media. The viscosity is given by

$$\mu^* = \mu_L \left(1 - \frac{min(f_s, f_{s,CO})}{f_{s,cr}}\right)^{-1.55} \tag{2.22}$$

where μ_L is the molecular viscosity of the liquid, μ^* is the total average viscosity of the mixture which may be increased by the turbulent viscosity in the turbulent model. f_s is the solid fraction; $f_{s,CO}$ is the cohesive solid volume fraction; $f_{s,CR}$ is the critical solid fraction. The formula above, Eq. (2.22), states that the average viscosity of fluid will raise as the solid fraction or sediment concentration increases until the solid fraction is equal to the cohesive solid fraction where the solid-like model activates and the fluid viscosity cannot increase; whereas when the solid fraction is equal to the critical solid fraction, the fluid viscosity becomes infinite which means that the complete status of solid forms, which is identical to the model of the drag coefficient. More in detail, note that the fluid viscosity μ^* in Eq. (2.22) is enhanced by increasing the suspended sediment concentration (SSC). This enhancement rises with SSC until $f_s = f_{s,CO}$ (defaulted as 0.15 in FLOW-3D). However, when the solid volume fraction (f_s) reaches or exceeds $f_{s,CO}$, (*i.e.,* $f_s \geq f_{s,CO}$), it will not cause the viscosity to rise any more; rather, the particles begin to interact with one another to cause solid-like behavior.

In addition, the viscosity and density are functions of the mud concentration, and they are calculated according to their magnitude. The fluid viscosity increases as the suspended concentration sediment(SCS) increase. This SCS can only be specified at boundaries where fluid crosses, and it is specified in units of mass/volume (*e.g.,* kg/m^3 the same units as density) in the units during the model setup. In this study, the deformable mud slide is represented by suspended mud, which advects and drifts

according to the fluid local pressure gradient (Flow Science, Inc, 2009). Drifting occurs in the suspended sediment, and sediment particles drift relative to the fluid due to the density difference between the sediment particles and the fluid. This velocity is computed as the balance between buoyant forces and the fluid's drag on the particle. The drag is computed with the assumption of Stokes flow, where the Reynolds number is low, *i.e.,* $Re << 1$ around spherical sediment particles. Drift is the settling of the sediment particles due to the buoyant force on the particle. Conversely, lifting occurs when the shear force outweighs the critical value for particles.

In FLOW-3D, in the diffusion/advection equation, those two components, drifting and lifting, are incorporated into the equation of motion with the effect of diffusion/advection as can be seen by

$$\underbrace{\left(\frac{\partial C_s}{\partial t}\right)_x}_{\text{(a)}} = \underbrace{D\nabla^2 C_s}_{\text{(b)}} - \underbrace{\mathbf{u}\cdot\nabla C_s}_{\text{(c)}} - \underbrace{\mathbf{u}_{drift}\cdot\nabla C_s}_{\text{(d)}} - \underbrace{\mathbf{u}_{lift}\cdot\nabla C_s}_{\text{(e)}}. \tag{2.23}$$

in which

(a) Rate of concentration change:

$$\left(\frac{\partial C_s}{\partial t}\right)_x$$

(b) Effect of diffusion:

$$D\nabla^2 C_s = D\left(\frac{\partial^2 C_s}{\partial x^2} + \frac{\partial^2 C_s}{\partial y^2} + \frac{\partial^2 C_s}{\partial z^2}\right) \tag{2.24}$$

(c) Effect of advection:

$$\mathbf{u}\cdot\nabla C_s = [u_x, u_y, u_z]\cdot\left[\frac{\partial C_s}{\partial x}, \frac{\partial C_s}{\partial y}, \frac{\partial C_s}{\partial z}\right] = u_x\frac{\partial C_s}{\partial x} + u_y\frac{\partial C_s}{\partial y} + u_z\frac{\partial C_s}{\partial z} \tag{2.25}$$

(d) Effect of drifting:

$$\begin{aligned}\mathbf{u}_{drift} \cdot \nabla C_s &= [u_{x,drift}, u_{y,drift}, u_{z,drift}] \cdot \left[\frac{\partial C_s}{\partial x}, \frac{\partial C_s}{\partial y}, \frac{\partial C_s}{\partial z}\right] \\ &= u_{x,drift}\frac{\partial C_s}{\partial x} + u_{y,drift}\frac{\partial C_s}{\partial y} + u_{z,drift}\frac{\partial C_s}{\partial z}\end{aligned} \tag{2.26}$$

(e) Effect of lifting:

$$\begin{aligned}\mathbf{u}_{lift} \cdot \nabla C_s &= [u_{x,lift}, u_{y,lift}, u_{z,lift}] \cdot \left[\frac{\partial C_s}{\partial x}, \frac{\partial C_s}{\partial y}, \frac{\partial C_s}{\partial z}\right] \\ &= u_{x,lift}\frac{\partial C_s}{\partial x} + u_{y,lift}\frac{\partial C_s}{\partial y} + u_{z,lift}\frac{\partial C_s}{\partial z}\end{aligned} \tag{2.27}$$

where C_s is the local concentration of the suspended sediment. D is a diffusion coefficient, which is set by users in FLOW-3D input file. $\mathbf{u}$ is the local fluid velocity of advection, and $\mathbf{u}_{lift}$ and $\mathbf{u}_{drift}$ are the local lifting and drifting velocities, respectively (Flow Science, Inc, 2009).

The drift velocity is

$$\mathbf{u}_{drift} = \frac{f_L \cdot {d_{50}}^2}{18\mu}\frac{\nabla P}{\overline{\rho}}(\rho_s - \rho_L) \tag{2.28}$$

where ρ_s is the sediment density while ρ_L is the density of the fluid. The liquid fraction, f_L, is a measure of the fraction of the total volume occupied by liquid; it is equal to $1 - f_s$. f_L is included in Eq. (2.28) because drifting is limited by the presence of solid, which means in regions where are full of solids (*i.e.*, $f_L = 0$), $\mathbf{u}_{drift}$ falls to zero. d_{50} is the mean sediment particle diameter, μ is the liquid viscosity and $\nabla P/\overline{\rho}$ is the mechanical potential gradient, or body acceleration.

The local mean density $\overline{\rho}$ is given by

$$\overline{\rho} = \rho_L + f_s(\rho_s - \rho_L) \tag{2.29}$$

where f_s is the solid fraction in the cell.

$$\mathbf{u}_{lift} = \alpha n_s \sqrt{\frac{\tau - \tau_{crit}}{\overline{\rho}}} \tag{2.30}$$

in which $\alpha(0 < \alpha < 1)$ is a dimensionless parameter representing probability that a particles are lifted away from the packed sediment surface, n_s is the normal vector to the packed bed surface. τ is the shear stress due to the fluid viscosity. τ_{crit} is the critical shear stress $(= \theta_{crit} g(\rho_s - \rho_L) d_{50})$, being with θ_{crit} critical shield parameter; g acceleration of gravity. It should be mentioned that $\mathbf{u}_{lift}$ is zero in the region where the local shear stress (τ) cannot exceed the critical, τ_{crit}, so there is no influence of lifting on the motion of the suspended sediment in the most flow domain except in the vincinity of the packed sediment interfaces.

In the Eq. (2.23), in order to find four unknowns, u_x, u_y, u_z and P, the momentum equation is utilized as

$$\underbrace{\frac{\partial \mathbf{u}}{\partial t}}_{\text{(a)}} + \underbrace{\mathbf{u} \cdot \nabla \mathbf{u}}_{\text{(b)}} = \underbrace{-\frac{\nabla P}{\overline{\rho}}}_{\text{(c)}} + \underbrace{\frac{\nabla \cdot \tau}{\overline{\rho}}}_{\text{(d)}} + \underbrace{\mathbf{g}}_{\text{(e)}} - \underbrace{K\mathbf{u}}_{\text{(f)}} \tag{2.31}$$

in which

(a) Rate of velocity change (acceleration):

$$\frac{\partial \mathbf{u}}{\partial t} = \frac{\partial u_x}{\partial t} i + \frac{\partial u_y}{\partial t} j + \frac{\partial u_z}{\partial t} k$$

(b) Advective acceleration:

$$\mathbf{u}\cdot\nabla\mathbf{u}$$
$$= u_x\left(\frac{\partial u_x}{\partial x}+\frac{\partial u_y}{\partial x}+\frac{\partial u_z}{\partial x}\right)i + u_y\left(\frac{\partial u_x}{\partial y}+\frac{\partial u_y}{\partial y}+\frac{\partial u_z}{\partial y}\right)j + u_z\left(\frac{\partial u_x}{\partial z}+\frac{\partial u_y}{\partial z}+\frac{\partial u_z}{\partial z}\right)k \tag{2.32}$$

(c) Pressure gradient:

$$\frac{\nabla P}{\overline{\rho}} = \frac{1}{\overline{\rho}}\left(\frac{\partial P}{\partial x}i+\frac{\partial P}{\partial y}j+\frac{\partial P}{\partial z}k\right) \tag{2.33}$$

(d) Stress gradient:

$$\frac{\nabla\cdot\tau}{\overline{\rho}}$$
$$= \frac{1}{\overline{\rho}}\left(\frac{\partial \tau_{xx}}{\partial x}+\frac{\partial \tau_{xy}}{\partial x}+\frac{\partial \tau_{xz}}{\partial x}\right)i + u_y\left(\frac{\partial \tau_{yx}}{\partial y}+\frac{\partial \tau_{yy}}{\partial y}+\frac{\partial \tau_{yz}}{\partial y}\right)j + u_z\left(\frac{\partial \tau_{zx}}{\partial z}+\frac{\partial \tau_{zy}}{\partial z}+\frac{\partial \tau_{zz}}{\partial z}\right)k \tag{2.34}$$

(e) Vector of gravity:

$$\mathbf{g} = g_x i + g_y j + g_z k \tag{2.35}$$

(f) Velocity vector multiplied by drag coefficient:

$$= K\left(u_x i + u_y j + u_z k\right). \tag{2.36}$$

Here, drag coefficient (K) among particles can be estimated as a function of solid volume fraction (f_s) using experimental data given by

$$K = \begin{cases} 0 & \text{if} \quad f_s < f_{s,CO} \\ \left[\frac{f_{s,CR}-f_{s,CO}}{f_{s,CR}-f_s}\right]\left[\frac{f_{s,CR}-f_{s,CO}}{f_{s,CR}-f_s}-1\right] & \text{if} \quad f_{s,CO} < f_s < f_{s,CR} \\ \infty & \text{if} \quad f_s > f_{s,CR} \end{cases} \tag{2.37}$$

where the solid fraction f_s is a measure of the fraction of the total volume that is occupied by the sediment; its value is derived from the solid fraction f_s is used for the viscosity and drag models. $f_{s,CO}$ is the cohesive solid volume fraction over which the interaction among particles occurs (defaulted as 0.15 in FLOW-3D). $f_{s,CR}$ is the critical solid fraction over which the fluid flow ceases and the sediment particles are completely bound together and behave as the solid-like mass (defaulted as 0.67 in FLOW-3D).

In Eq. (2.31), there are four unknowns, u_x, u_y, u_z and P, and we can also mobilize four equations from Eq. (2.31) given by

$$\frac{\partial u_x}{\partial t} + u_x \frac{\partial}{\partial x}(u_x + u_y + u_z) = \frac{1}{\overline{\rho}} \left(-\frac{\partial P}{\partial x} + \frac{\partial}{\partial x}(\tau_{xx} + \tau_{xy} + \tau_{xz}) \right) + g_x - K u_x \quad (2.38)$$

$$\frac{\partial u_y}{\partial t} + u_y \frac{\partial}{\partial y}(u_x + u_y + u_z) = \frac{1}{\overline{\rho}} \left(-\frac{\partial P}{\partial y} + \frac{\partial}{\partial y}(\tau_{yx} + \tau_{yy} + \tau_{yz}) \right) + g_y - K u_y \quad (2.39)$$

$$\frac{\partial u_z}{\partial t} + u_z \frac{\partial}{\partial z}(u_x + u_y + u_z) = \frac{1}{\overline{\rho}} \left(-\frac{\partial P}{\partial z} + \frac{\partial}{\partial z}(\tau_{zx} + \tau_{zy} + \tau_{zz}) \right) + g_z - K u_z \quad (2.40)$$

$$\frac{\partial u_x}{\partial x} + \frac{\partial u_y}{\partial y} + \frac{\partial u_z}{\partial z} = 0 \qquad \text{(When eroding fluid is incompressible)} \quad (2.41)$$

By using above four equations along with boundary and initial conditions, FLOW-3D evaluates the four unknowns. FLOW-3D estimates unknown τ in Eq. (2.30) as well.

3. NUMERICAL MODELING IMPLEMENTATION

3.1 Introduction

Tsunami wave generation by landslides is a complex phenomenon with the granular materials, water and air interacting with each other during the impact to the water body and wave generation process. In this chapter, the physical model and experiments applied in this study are described, along with the techniques used to couple both numerical models (TSUNAMI3D and FLOW-3D) to simulate tsunami wave generation induced by subaerial landslides.

3.2 The Physical Model and Experiments

The physical experiments based on the generalized Froude-similarity were conducted at the Network for Earthquake Engineering Simulation (NEES) Tsunami Wave Basin at the O. H. Hinsdale Wave Research Laboratory at Oregon State University in Corvallis by a tsunami research team led by Dr. Hermann Fritz, Georgia Institute of Technology (Mohammed et al., 2011). The experimental data have been obtained from performing tests reproducing waves generated by deformable granular landslides on a slope which impact the water surface and thereby generate tsunami waves as seen in Fig. 3.1 for three basic domain configurations: fjord like, headland, and farfield coastline, as shown in Fig. 3.2, 3.3, 3.4, respectively. Particle image velocimetry (PIV) analysis was used to record the surface velocity of the subaerial granular landslide motion. A snapshot of the physical experiment is shown in Fig. 3.1 at the moment the subaerial landslide is impacting the water body.

Three-dimensional physical experiments (fjord-like, headland and farfield coastline) were constructed in the wave basin with a sliding slope of $\alpha = 27.1°$. The subaerial slide source with a total of mass of 1350 kg is modeled using naturally

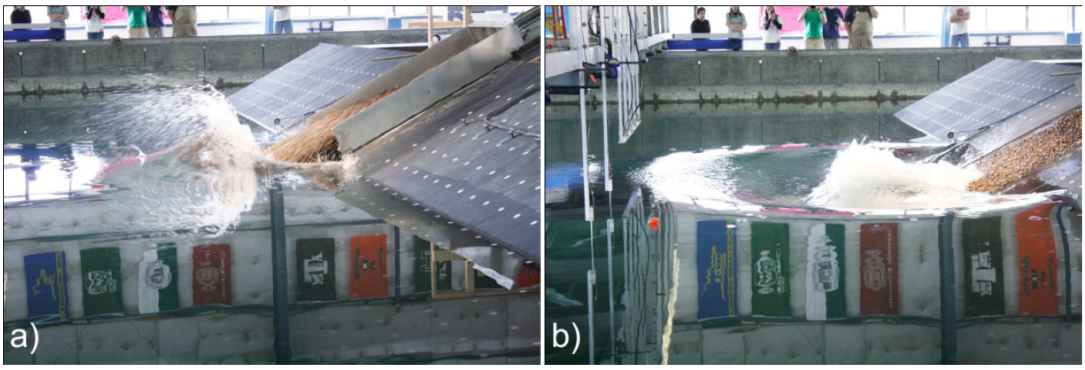

Figure 3.1: (a) Water displacement during landslide impact with the water body, (b) leading radial wave propagation and trailing wave formation (Mohammed et al., 2011).

rounded river gravel with $d_{50} = 13.7\ mm$, grain density of $\rho_g = 2600\ kg/m^3$, bulk slide density of $\rho_s = 1760\ kg/m^3$, porosity of 0.31, internal friction angle of $\varphi = 41°$ and basal friction angle of $\delta = 23°$. Others parameters of the landslide experiments are: water depth of 0.6 m, landslide volume of $V_s = 0.756\ m^3$, landslide release velocity from the slide box on the slope of $v_b = 3.8\ m/s$, and landslide impact velocity at the water surface of $v_s = 5.5\ m/s$. An array of wave gauges in the basin measures the wave profiles and wave runups on the opposite slope or at the lateral side to the subaerial landslide generation area for each of the basin configurations (fjord, headland and far field coastline) with the number of sensors being 26 for the fjord; 37 for the headland; 34 for the far field case, see Fig. 3.2, 3.3, 3.4, respectively.

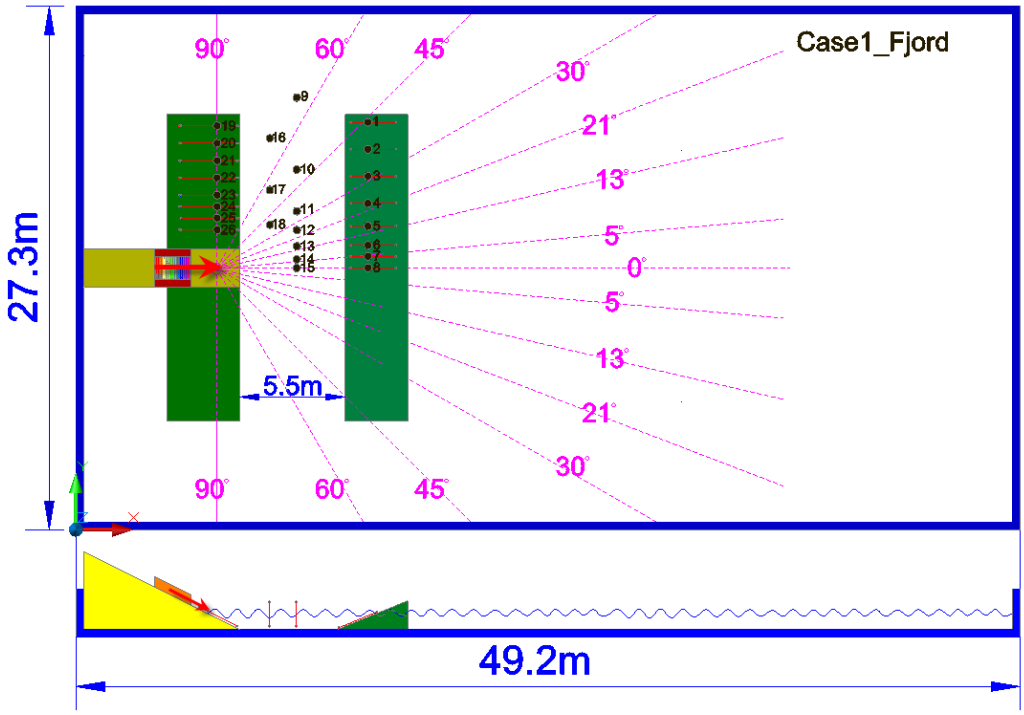

Figure 3.2: Experimental setups for a fjord with a straight opposing coastline

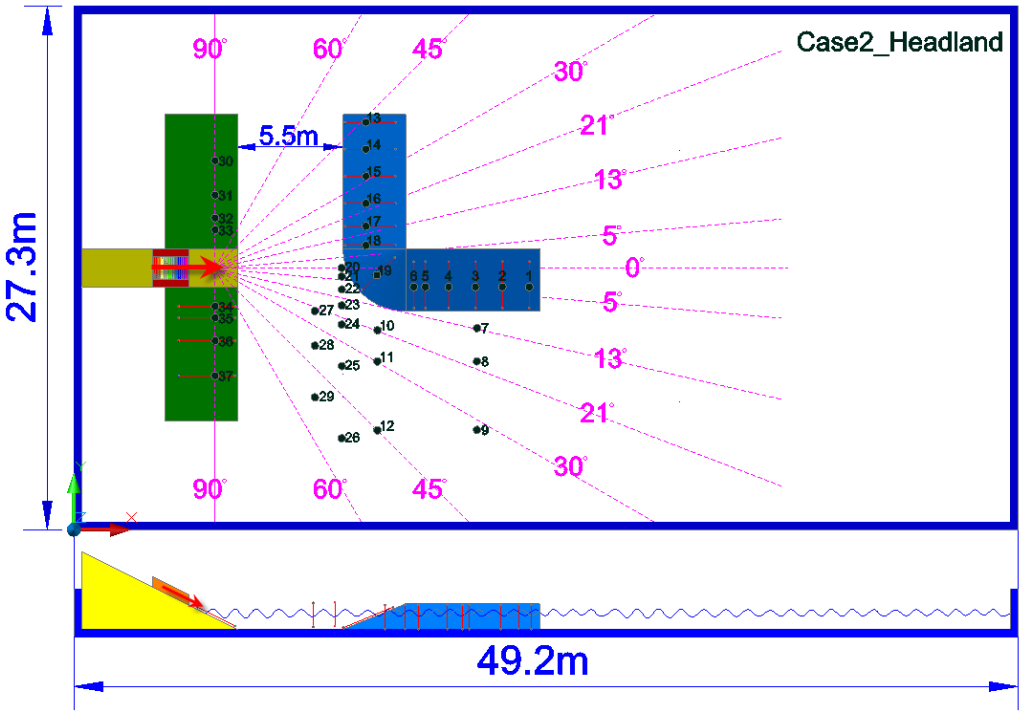

Figure 3.3: Experimental setups for a headland with 90° bended coastline

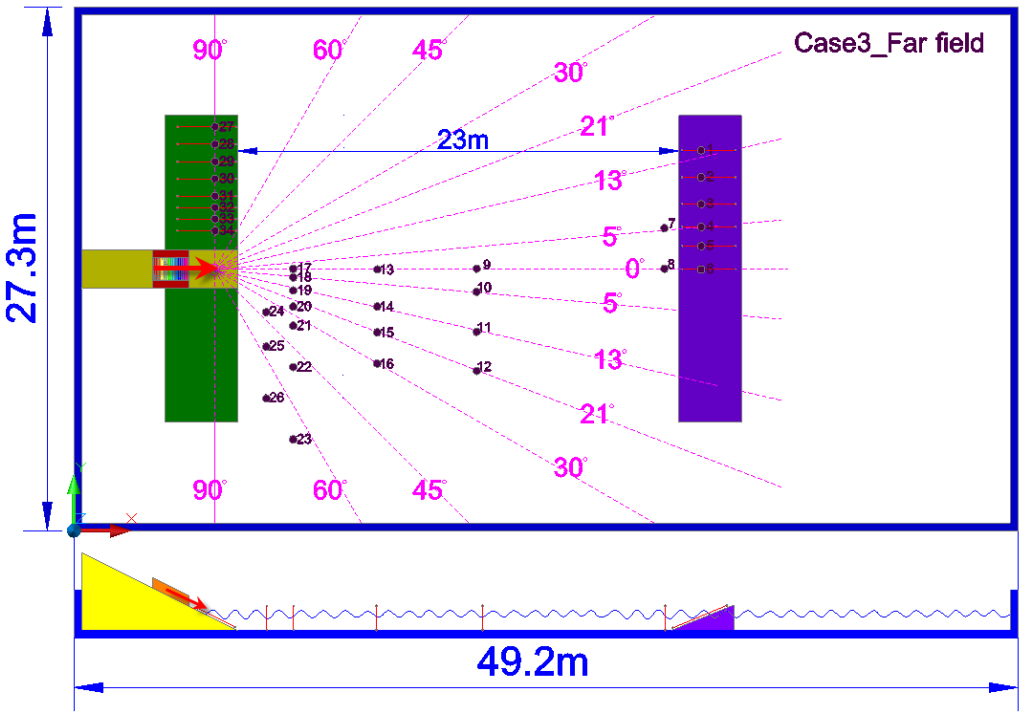

Figure 3.4: Experimental setups for a farfiled with a straight opposing far field coastline

3.3 The Numerical Models

In this work, we apply the fully three-dimensional computational fluid dynamics models, TSUANMI3D and commercial code FLOW-3D, to simulate waves generated by deformable subaerial landslides and we compare the results against available experimental data to validate the models. The models solves the Navier-Stokes equations and the continuity equation for incompressible flow along with the volume of fluid method (VOF) to compute the free surface motion. Some of research based on the commercial CFD code FLOW-3D have alreadt been presented in the field of tsunami works by Choi et al. (2007) and Montagna et al. (2011). TSUNAMI3D and FLOW-3D have been used to reproduce the experiments of Mohammed et al. (2011).

3.3.1 Methodology: Geometry and Grid

Grid resolution and initial time step strongly affect numerical results. Both models allow to divide the domain into several grids of different resolution or to use nested grids. Beside, the time-step size is variable and adjusted by respecting the Courant limit (N_{CFL}), as mentioned in previous Section 2.10. The minimum time step depends on its initial value and can be selected by the user. As part of the bathymetry configuration of simulation, the geometry was generated using AutoCAD, based on the dimensions of the physical model. For TSUNAMI3D, it was used into the code as ASCII files which is saved as x, y, z topographic data through griding of triangulation with linear interpolation from Surfer 9, Golden software, whereas the full geometry was incorporated into FLOW-3D through stereo-lithography (STL) files directly. As part of boundary conditions for the wave basin, as seen in App. $A.1 \sim A.6$, the rigid walls of wave basin are labeled as "W" which implies that all velocity derivatives across the wall are zero. On the other hand, in the x-direction, continuative outflow boundaries, "C", was selected on the other side of the boundary, where fluid is to

flow smoothly out of the mesh for a problem for incompressible flow calculations. Beside, for numerical efficiency for both models, the domain in the x-direction is reduced by cutting it at 20 m for the fjord; 30 m for the headland; and 37 m for the farfield case. This is achieved during the process of models' numerical validation by means of identifying best methodologies and critical soil parameters. For the application of the numerical models, TSUNAMI3D's impacting material (mud) is modeled as Newtonian fluid with a bulk density of 2600 kg/m^3, kinematic viscosity of $\nu_{mud} = 10^4 \times \nu_{water}$, Coulomb internal and basal friction of 35° and 25° respectively. On the other hand, for FLOW-3D, the deformable slide is represented by the suspended mud approximation with parameters: diameter of mud particles of $\phi = 13.7\ mm$, mud bulk density of 2600 kg/m^3, Suspended Sediment Concentration (SSC) of 2550 kg/m^3, angle of repose which is the maximum slope steepness that can be held without the sediment pile falling to a lower energy state (lower angle) of 41°. The present study aims to find the most appropriate approach for calculation of subaerial landslide-induced tsunami.

3.3.2 Methodology: Mesh Convergence Test

Fig. 3.5 displays wave profiles at gauge number 15 of the fjord case, in order to compare the numerical results, in specific FLOW-3D, obtained with four meshes of 3 $cm \times 3\ cm \times 3\ cm$; 4 $cm \times 4\ cm \times 4\ cm$; 5 $cm \times 5\ cm \times 5\ cm$; and 6 $cm \times 6\ cm \times 6\ cm$ in the x, y, and z direction, respectively. Results show the condition pertaining to a reasonable state. Although the four meshes yield virtually that the smaller size of mesh, the lower the leading wave height, a mesh-converged solution was attained (we were not interested in obtaining the mesh convergence rate). For numerical efficiency, *i.e.,* the total number of computational cells, the mesh with 4 $cm \times 4\ cm \times 4\ cm$ was then used through for all the simulated cases.

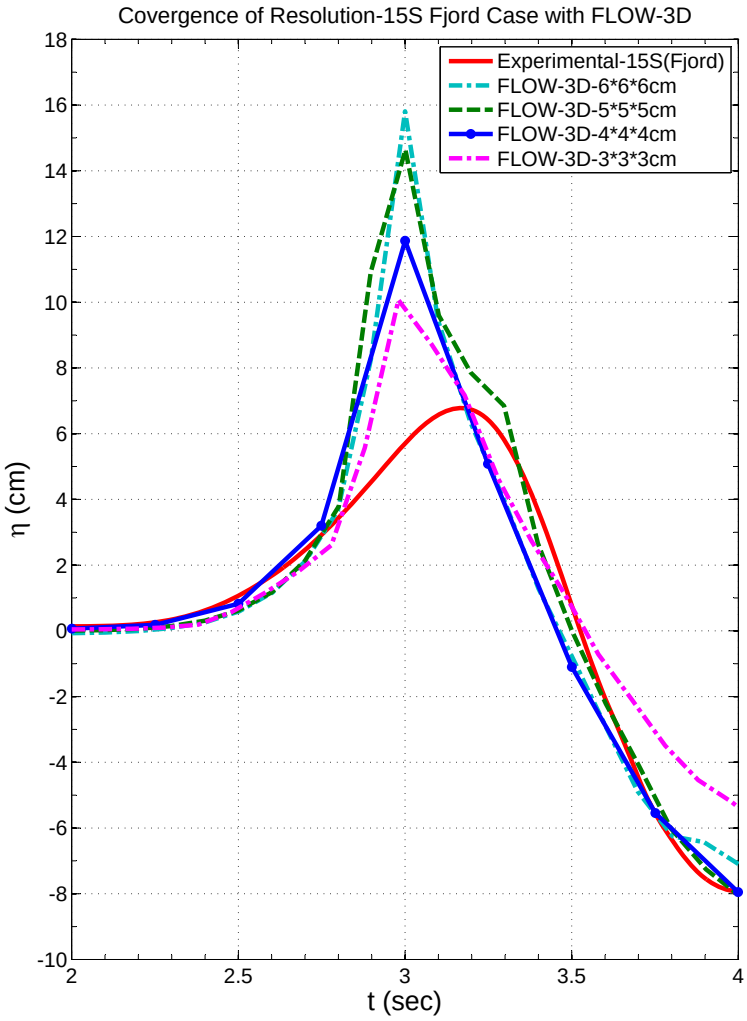

Figure 3.5: Results of mesh convergence test: comparison of results for four meshes of 3, 4, 5, and 6 cm

4. MODEL RESULTS

When a landslide penetrates the water body, it pushes ahead the fluid and a leading positive outward radial propagating waves wave is generated. Once the landslide becomes totally submerged, the water is initially depressed by generating a trailing wave through. Strong lateral free surface gradients occur in the generation area, where splashes take place, resulting in converging flows that collide and rebound along the centerline of the landslide. The rebound is the responsible of a large positive wave radiating to farfield.

4.1 Overview of the Numerical Results

In this Chapter, the results of the numerical models are compared with the experimental measurements. In the work described herein, we used the experimental data collected by means of the sensors depicted in Fig. 3.2, 3.3, 3.4 and then summarized in Table 4.1, 4.2, and 4.3 that consist of water level and runup up profile time series. Note that S indicates free surface elevation (sea-level gauge) and R is runup gauge.

Table 4.1: Sensor names and location of fjord case

Sensor name	$x(m)$	$y(m)$	$r(m)$	$\theta(^\circ)$
Water level gauges				
15S	11.5	13.67	4.14	0
Runup gauges				
8R	13.5	13.67	9.16	0
23R	7.36	17.47	3.78	-90
26R	7.36	15.66	1.98	-90

In this study, two different coordinate systems are used. For representing the topography system, the origin is fixed at bottom-left of water tanks (0, 0) in the direction of x and y, as shown in Fig. 3.2, 3.3, and 3.4. In addition, a cylindrical coordinate system where the origin may be fixed at the impact location or intersection of the waterline with the hill slope. The waves η are defined as a function of $f(r, \theta, t)$, where r is the distance from the origin relative to the landslide. The landslide direction is from $\theta = +90^{\circ}$ to -90°.

Table 4.2: Sensor names and location of headland case

Sensor name	$x(m)$	$y(m)$	$r(m)$	$\theta(^{\circ})$
Water level gauges				
10S	15.82	10.42	9.06	+21
Runup gauges				
31R	7.36	17.47	3.78	-90
33R	7.36	15.66	1.98	-90

Table 4.3: Sensor names and location of farfield case

Sensor name	$x(m)$	$y(m)$	$r(m)$	$\theta(^{\circ})$
Water level gauges				
8S	30.77	13.67	23.42	0
15S	15.82	10.36	9.06	+21
17S	11.42	13.67	4.14	0
Runup gauges				
6R	32.69	13.67	25.33	0
31R	7.36	17.47	3.78	-90
33R	7.36	15.66	1.98	-90

4.2 Comparison of Numerical and Experimental Time Series

It has to be stressed that, as stated in the previous Section 3.3.1, the use of reflective boundaries as walls in the wave basin has produced reflected waves that have contaminated the wave field around the islands after the three-four waves have passed. Hence, the validation of the numerical models has been carried out by focusing on the first two waves and inducing the maximum runup in the area between -90° and 0° from the impact point, which is the area considered in this study for comparison with the experiments. Water free surface elevation and wave runup comparisons were performed using TSUNAMI3D and FLOW-3D numerical models.

4.2.1 Fjord Case

The fjord configuration traps the wave energy between the two facing slopes and slowly disperses the energy laterally through the fjord channel. The superposition of reflected waves results in complex oscillation and wave patterns that are very challenging for any three dimensional models to reproduce accurately. Fig. 4.1 shows the comparison between numerical results and experimental results with the time series. The first wave is generated by a piston-like mechanism. Fig. 4.1 shows models and experiment results for the surface elevation at gauge $15S$ (see also Fig. 3.2 and Table 4.1 for gauge location). Gauge $15S$ is placed at the distance $r = 4.14\ m$, $\theta = 0^\circ$ from the generation area, in which the landslides impact the water body at the water depth of $h = 0.6\ m$. In the presence of the fjord, the main reflected wave from the fjord slope reaches the propagating wave around the sixth wave, as seen in the figure. The sixth crest corresponds to the wave reflection from the opposite-facing fjord slope in the opposite direction of the outward wave propagation. The second panel of Fig. 4.1 shows the wave runup profile recorded along the opposite-facing slope (wave runup gauge $8R$) in the direction of the subaerial landslide motion,

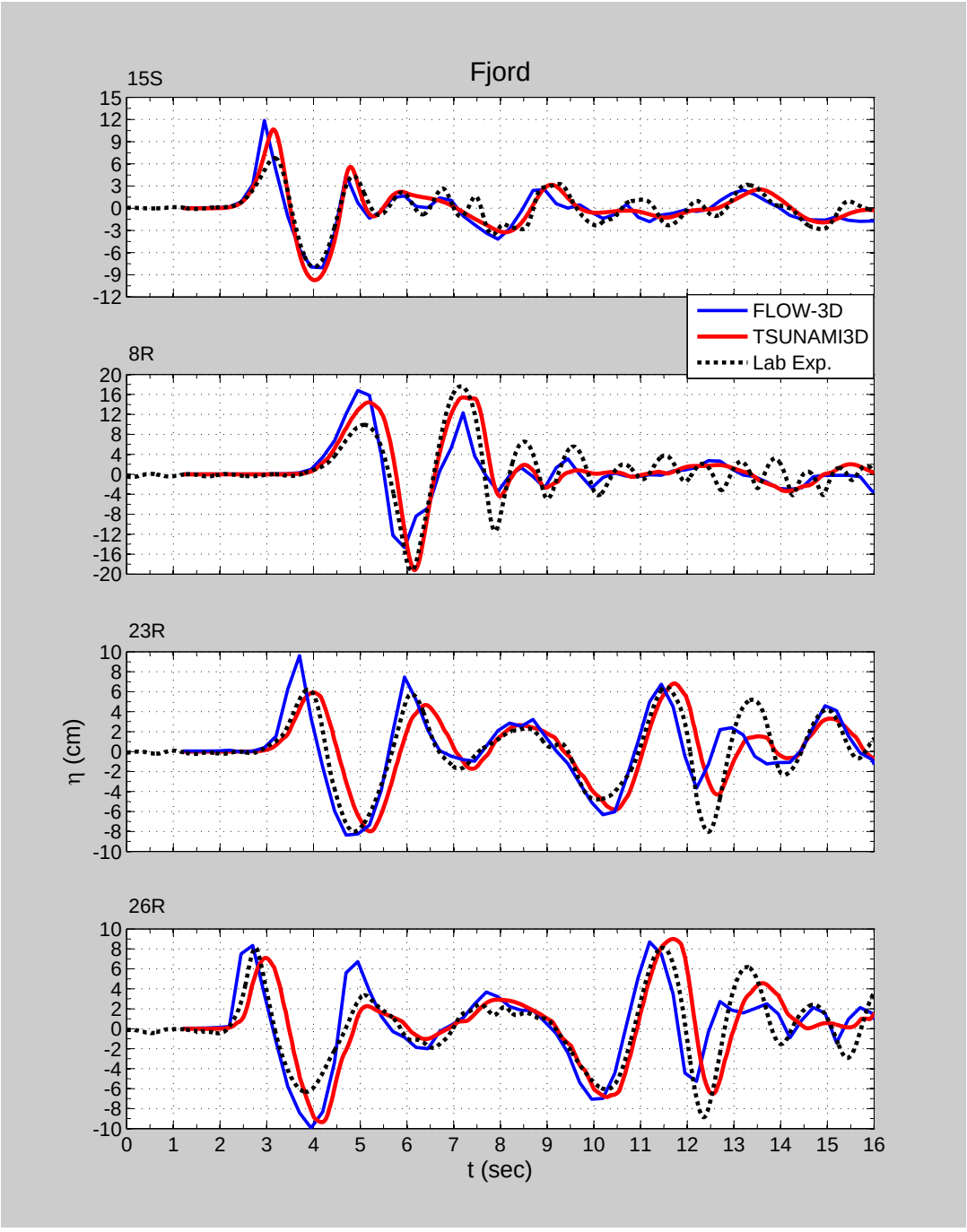

Figure 4.1: Comparison of free surface elevations and wave runup profiles with time series for fjord case: *dashed lines* indicate experimental data; *continuous blue lines* represnt numerical results for FLOW-3D; and *continuous red lines* numerical results for TSUNAMI3D

$\theta = 0°$. It presents that a crest is very steep, followed by a larger trough. At this runup gauge, the trough of the second wave increases as the crest of the first wave is smaller compared with the second one. The third and fourth panels show wave runup time series recorded at gauges located to the side of the sliding slope, $\theta = -90°$. For the gauges $23R$ and $26R$, reflected waves from the water tank wall boundary come back to the fjord slope and hill slope after about 11 second of the time series. Overall agreement in the models' wave pattern with respect to laboratory experiment is reasonably too.

4.2.2 Headland Case

The setup of the headland case is similar to half of the fjord setup. A 90 degree curvature with the radius 3.26 m in the opposite-facing headland slope is located in the direction of the landslide motion. Fig. 4.2 shows models and experimental results for the surface elevation at gauge $10S$, $(r,\ \theta) = (9.06\ m,\ +21°)$ and wave runup gauges, $31R$ and $33R$, recorded along the side of the sliding slope, $\theta = -90°$. The gauge $10S$ is located near the bended island. In the presence of the headland, the first two crests generate with the undisturbed wave. The energy of the generated waves is funneled by the curved headland area and then amplifies the wave as seen in the third wave. Compared with the fjord case, the headland configuration traps only part of the wave energy in the channel and radiates the rest of the energy into the open water basin. Similar to the results of the fjord case, gauges $31R$ and $33R$, reflected waves from the water tank wall boundary come back to the islands after about 11 s. The wave runup along the the sliding slope can be amplified due to the trapped energy by the wave reflection from the headland slope.

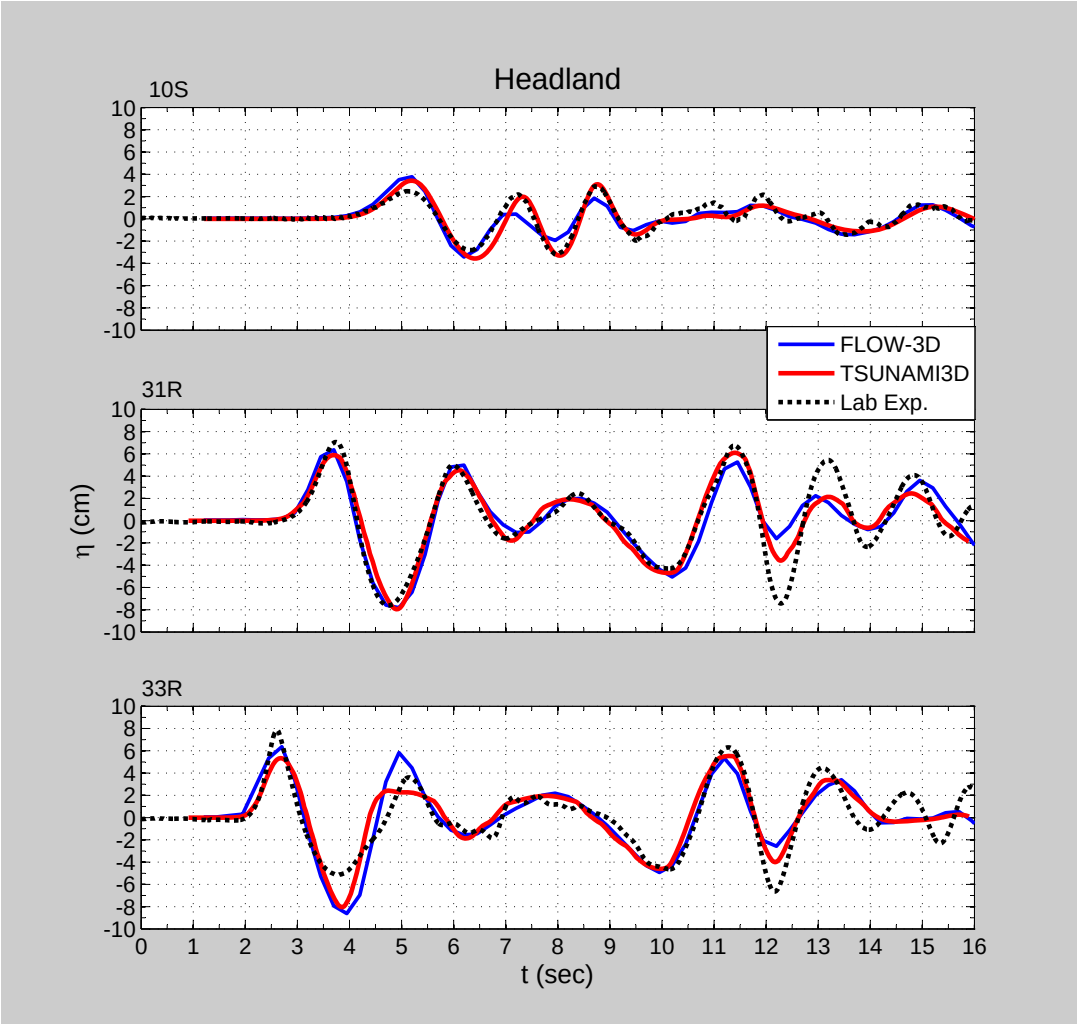

Figure 4.2: Comparison of free surface elevations and wave runup profiles with time series for headland case: *dashed lines* indicate experimental data; *continuous blue lines* represnt numerical results for FLOW-3D; and *continuous red lines* numerical results for TSUNAMI3D

4.2.3 Farfield Case

The setup of the farfield case is also similar to the fjord setup, but the opposite-facing slope is far away at the distance about 23 m from the side of the sliding slope. The time series in Fig. 4.3 show the models and experiment results for the surface elevation, for all the gauges. The second panel of Fig. 4.3 shows that the generated wave has fourth or fifth wave crests and coincides with the undisturbed wave with the absence of a headland for $15S$, which is located as the same location of $10S$ of headland case, $(r,\ \theta) = (9.06\ m,\ \ +21^{\circ})$. By looking at the third panel for $17S$ in above the figure, we can see that in the absence of the fjord island, the undisturbed wave is sustained until the sixth peak, after which wave reflections from the back and the side of the water tank walls interfere with the propagating wave. Fig. 4.4 shows models and experiment results for wave runup gauges on Farfield coastline: $6R$ which is located in the opposite-facing slope in the direction of the subaerial landslide motion, $(r,\ \theta) = (25.3\ m,\ 0^{\circ})$ and $31R$ and $34R$ that recorded along the side of the sliding slope, $\theta = -90^{\circ}$. As can be seen in Figs. 4.3 and 4.4, overall agreement between the models is very good despite the different methodologies applied in them.

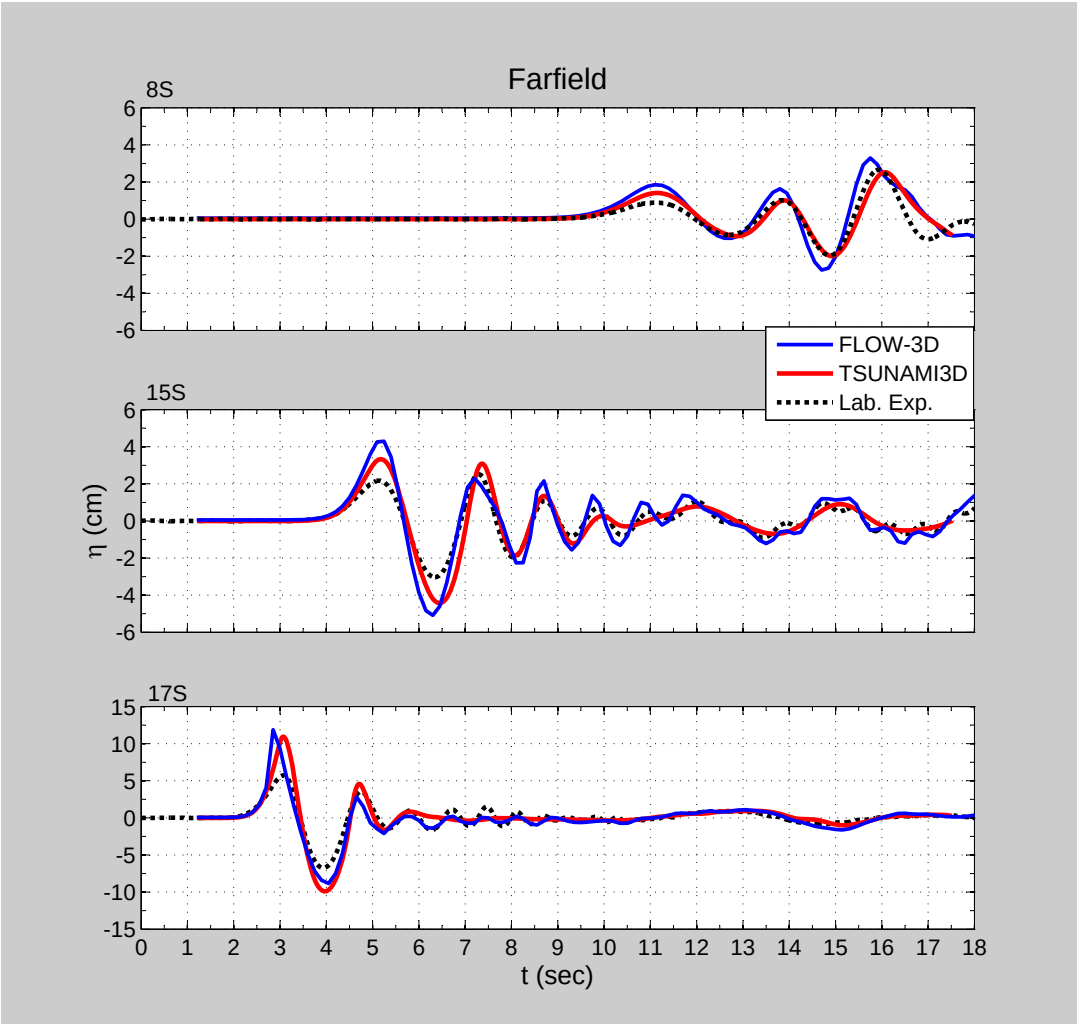

Figure 4.3: Comparison of free surface elevations with time series for farfield case: *dashed lines* indicate experimental data; *continuous blue lines* represnt numerical results for FLOW-3D; and *continuous red lines* numerical results for TSUNAMI3D

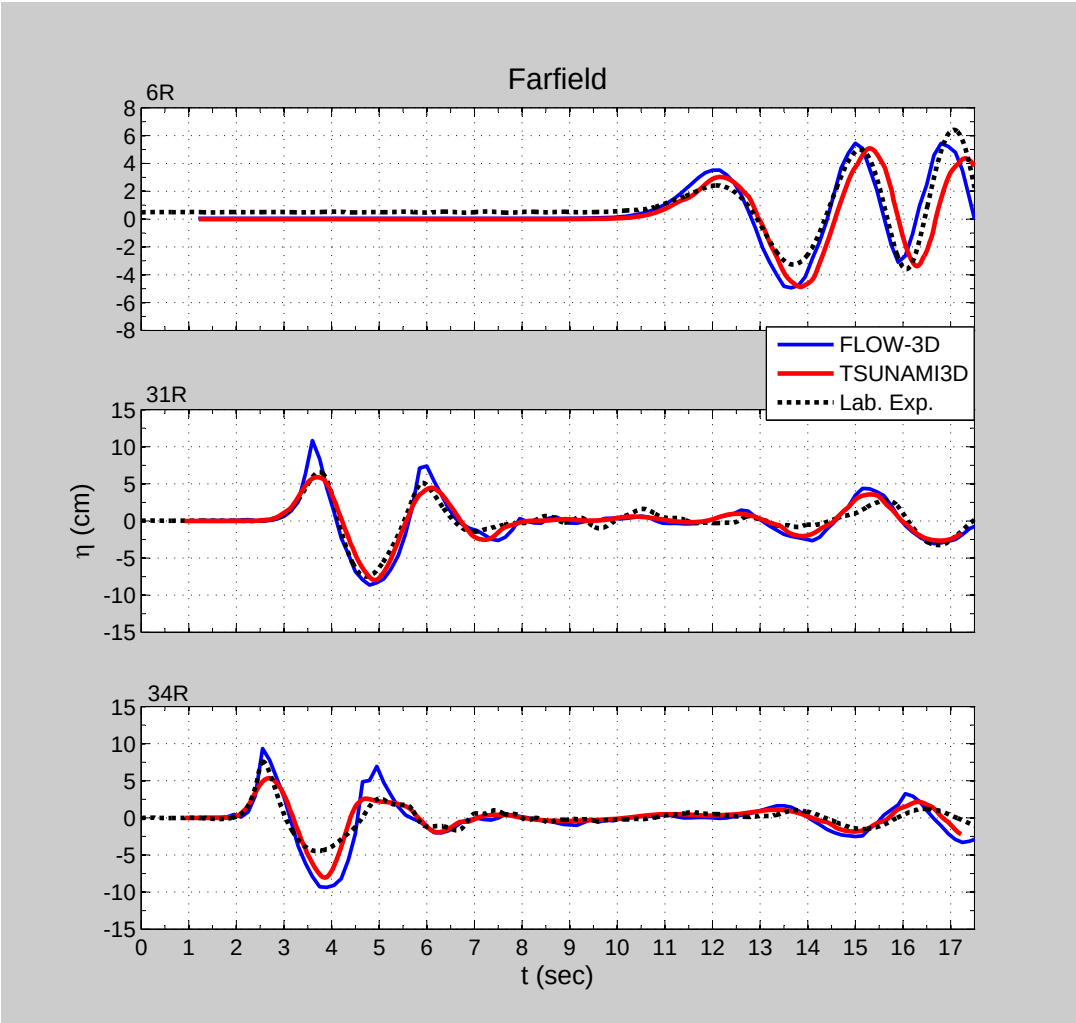

Figure 4.4: Comparison of wave runup profiles with time series for farfield case: *dashed lines* indicate experimental data; *continuous blue lines* represnt numerical results for FLOW-3D; and *continuous red lines* numerical results for TSUNAMI3D

4.3 Validation of the Numerical Models: Comparison for Error

The normalized error (ERR) shown in Table 4.4 is used to measure model accuracy in time. The ERR is defined as

$$ERR = \frac{|\zeta_{ex,i} - \zeta_{mo,i}|}{\zeta_{ex_{max}} - \zeta_{ex_{min}}} \tag{4.1}$$

ERR is the accumulative error between the values predicted by the model (ζ_{mo}) and the values observed in the physical experiment (ζ_{ex}). The error is normalized with respect to the distance between the maximum and minimum values obtained in the lab experiment ($\zeta_{ex_{max}} - \zeta_{ex_{min}}$), which usually corresponds to the first or second wave height. The negative value of ERR represents that the result is underpredicted, whereas the positive value indicates the result is overpredicted. The largest crest during the experiments has been observed at gauge $15S$ as 6.8 cm for the fjord case; $17S$ as 5.7 cm for the farfield case, which is placed very close to the impact area that generated initial wave propagation. Generally, in the tsunami simulation, the crest of water height is more important to consider than trough height. With respect to the laboratory experimentation, models reasonably well predict the wave pattern; however, they overpredicted the positive wave by 34.4% for FLOW-3D and 26.2% for TSUNAMI3D (error has been normalized by the laboratory experiment wave height(crest-trough) $= 6.8 - (-7.9) = 14.7$). In addition, it should be mentioned that in general, granular landslides seem to generate lower waves compared with solid one, which has no porosity in the landslide material adapted in the numerical simulations, as indicated by Zweifel (2004). Furthermore, it is important to distinguish a slide impact zone to decay the induced wave height faster due to air entrainment, large turbulence production, amplitude dispersion and frequency dispersion, specifically, in the case of subaerial landslides generated water motions. The models' overprediction

Table 4.4: The normalized error for the maximum wave height of fjord case

Domain Configuration	**The Normalized Error (ERR)**			
	+Positive (CREST)		-Negative (TROUGH)	
	TSUNAMI3D	FLOW-3D	TSUNAMI3D	FLOW-3D
Fjord				
15S (CR)	26%	34%	-12%	-1%
8R (FR)	-6%	-2%	-1%	13%
23R (CR)	-2%	24%	0%	-2%
26R (CR)	-7%	1%	-20%	-25%
Headland				
10S (FR)	18%	25%	-15%	-13%
31R (CR)	-8%	-5%	-2%	-1%
33R (CR)	-11%	-19%	-27%	-22%
Farfield				
8S (FR)	16%	-1%	-17%	-1%
15S (CR)	41%	22%	-40%	-27%
17S (CR)	52%	43%	-20%	-32%
6R (FR)	-20%	-10%	2%	5%
31R (CR)	-5%	44%	-44%	-50%
34R (CR)	-19%	15%	-30%	-40%

*(CR) : Gauge location close to the generation region
*(FR) : Gauge location far from the generation region

is attributed to the complex turbulence process and air entrainment at the impact of the granular material as mentioned in the Chapter 1, *e.g.,* Fritz et al. (2001, 2003a,b); Walder et al. (2003); Hoque and Aoki (2008); Heller et al. (2008); Heller and Harger (2010), and the numerical simulations studied by Monaghan and Kos (2000), Mader and Gittings (2002) and Panizzo et al. (2005b). As far as the maximum wave height during the experiments is concerned along the side of the sliding slope, $\theta = -90°$, wave runup reaches its maximum at the second gauge: $26R$ as 8.1 cm for the fjord; $33R$ as 7.9 cm for headland case; and $34R$ as 7.6 cm for farfield case, which is close to the landslide source and the impact region. For fjord case, models underpredicted the maximum crest wave runup by 7.1% for TSUNAMI3D and overpredicted by

1.5% for FLOW-3D. On the other hand, at gauge $23R$ (located in the outer sliding slope), the maximum runup errors are overpredicted by 23.8% for FLOW-3D and underpredicted by 2.1% for TSUNAMI3D.

In summary, overall numerical results agree satisfactorily with the experimentation and the general patterns on the free surface elevations and runups were reproduced with accuracy.

5. CONCLUSIONS

Tsunami wave generation by subaerial landslides is a complex phenomenon due to the interaction of granular materials, water and air during the impact process. In this study, we have integrated laboratory-scale experiments of tsunami generation by subaerial landslide with numerical models for three large scale landslide scenarios that were selected from a set of laboratory experiments, namely, fjord, headland, and far field coastline configuration. The work focuses on the numerical validation of two three-dimensional Navier-Stokes (3D-NS) models, FLOW-3D and our numerical model TSUNAMI3D. Both models are able to consider soil rheology on complex domain geometry to simulate waves generated by deformable subaerial landslides. TSUNAMI3D uses a Direct Numerical Simulation (DNS) or eddy viscosity approach, considering basal friction and internal friction, whereas the sediment scour model approach is used for FLOW-3D.

Outward radial propagating waves are generated when the water body is disturbed by the subaerial landslides. Once the landslide becomes totally submerged, the water is initially depressed by a trailing wave trough. Strong lateral free surface gradients occur in the generation area where the water splashes occur, resulting in converging flows that collide and rebound along the line of symmetry of the landslide. The rebound wave then results in a large positive wave radiating out to the far field and to the near field shore. Close examination of the numerical results of the models have shown that complex wave fields can be generated by subaerial landslides. It had been observed in the set of numerical experiments that the fjord configuration traps the wave energy between the two facing slopes and later is slowly drained laterally through the fjord channel. The highest waves propagate along the direction of the

slide motion. Comparisons have been performed between these numerical results and laboratory experiments to validate the models at various locations (gauges) for free surface and runup. In general, both 3D-NS models have been successfully applied to deformable subaerial landslides impacting the water to obtain wave characteristics in the far and nearby fields from the generation regions.

The leading wave resulting from the subaerial landslide impact region (at early stage of the wave evolution and close to the generation region) is overestimated by both models. The difference is mainly attributed to the simplification of the model to account for energy loss due to air entrainment, turbulence and to the time scale and spatial resolution applied. At later stage of the wave evolution, the superposition of reflected waves results in a complex oscillation and wave patterns, which seem to be accurately reproduced by both 3-D NS models, especially far from the generation region.

REFERENCES

Abadie, S., Morichon, D., Grilli, S., and Glockner, S. (2010). Numerical simulation of waves generated by landslides using a multiple-fluid Navier-Stokes model. *Coastal Engineering*, 57(9):779–794.

Assier-Rzadkiewicz, S., Mariotti, C., and Heinrich, P. (1997). Numerical simulation of submarine landslides and their hydraulic effects. *Journal of Waterway, Port, Coastal and Ocean Engineering, ASCE*, 123(4):149–158.

Ataie-Ashtiani, B. and Nik-Khah, A. (2008). Impulse waves caused by subaerial landslides. *Environmental Fluid Mechanics*, 8(3):263–280.

Bruschi, R., Bughi, S., Spinazzè, M., Torselletti, E., and Vitali, L. (2006). Impact of debris flows and turbidity currents on seafloor structures. *Norwegian Journal of Geology*, 86:317–337.

Choi, B. H., Kim, D. C., Pelinovsky, E., and Woo, S. B. (2007). Three dimesional simulation of tsunami run-up around conical island. *Coastal Engineering*, 54(374):618–629.

Di Risio, M. (2005). *Landslide generated impulsive waves: generation, propagation and interaction with plane slopes-an experimental and analytical study*. PhD thesis, University of Roma Tre, Rome.

Di Risio, M., Bellotti, G., Panizzo, A., and Girolamo, P. D. (2009). Three-dimensional experiments on landslide generated waves at a sloping coast. *Coastal Engineering*, 56(5-6):659–671.

Di Risio, M., De Girolamo, P., and Beltrami, G. (2011). Forecasting landslide generated tsunami: A review. In Mörner, N.-A., editor, *The Tsunami Threat - Research and Technology*, chapter 6, pages 81–106. InTech.

Di Risio, M. and Sammarco, P. (2008). Analytical modeling of landslide-generated waves. *Journal of Waterway, Port, Coastal and Ocean Engineering, ASCE*, 134:53–60.

Enet, F. and Grilli, S. T. (2007). Experimental study of tsunami generation by three dimensional rigid underwater landslides. *Journal of Waterway, Port, Coastal and Ocean Engineering, ASCE*, 133 (6):442–454.

Flow Science, Inc (2009). *FLOW-3D User's Manual Version 9.4*. Santa Fe, N.M.

Fritz, H. M. (2002). *Initial phase of landslide generated impulse waves*. PhD thesis, Versuchsanstalt für Wasserbau, Hydrologie und Glaziologie, ETH Zürich, Swiss ETH No. 14'871. Swiss Federal Institute Technology, Zürich.

Fritz, H. M., Hager, W. H., and Minor, H.-E. (2001). Lituya Bay case: rockslide impact and wave run-up. *Science of Tsunami Hazards*, 19(1):3–22.

Fritz, H. M., Hager, W. H., and Minor, H.-E. (2003a). Landslide generated impulse waves. 1. instantaneous fow fields. *Experiments in Fluids*, 35:505–519.

Fritz, H. M., Hager, W. H., and Minor, H.-E. (2003b). Landslide generated impulse waves. 2. hydrodynamic impact craters. *Experiments in Fluids*, 35:520–532.

Fritz, H. M., Hager, W. H., and Minor, H.-E. (2004). Near field characteristics of landslide generated impulse waves. *Journal of Waterway, Port, Coastal and Ocean Engineering, ASCE*, 130(6):287–302.

Fritz, H. M., Mohammed, F., and Yoo, J. (2009). Lituya Bay landslide impact generated mega-tsunami 50th anniversary. *Pure and Applied Geophysics*, 166(1-2):153–175.

Gisler, G., Weaver, R., and Gittings, M. L. (2006). Sage calculations of the tsunami threat from La Palma. *Science of Tsunami Hazards*, 24(4):288–301.

Gisler, G., Weaver, R., Mader, C., and Gittings, M. L. (2004). Two- and three-dimensional asteroid impact simulations. *Computing in Science Engineering*, 6(3):46–55.

Gitting, M. L. (1992). SAIC's adaptive grid eulerian code. *Defense Nuclear Agency Numerical Methods Symposium*, 1:28–30.

Grilli, S., Vogelmann, S., and Watts, P. (2002). Development of a 3D numerical wave tank for modeling tsunami generation by underwater landslides. *Engineering Analysis with Boundary Elements*, 26:301–313.

Grilli, S. T. and Watts, P. (1999). Modeling of waves generated by a moving submerged body. application to underwater landslides. *Engineering Analysis with Boundary Elements*, 23:645–656.

Grilli, S. T. and Watts, P. (2005). Tsunami generation by submarine mass failure. i: modeling, experimental validation and sensitivity analysis. *Journal of Waterway, Port, Coastal and Ocean Engineering, ASCE*, 131(6):283–297.

Harbitz, C., Pedersen, G., and Gjevik, B. (1994). Numerical simulations of slide generated water waves. *Journal of Hydraulic Engineering, ASCE*, 119(12):15–23.

Harlow, F. H. and Welch, J. E. (1965). Numerical calculation of time-dependent

viscous incompressible flow of fluid with a free surface. *The Physics of Fluids*, 8:2182–2189.

Heinrich, P. (1992). Nonlinear water waves generated by submarine and aerial landslides. *Journal of Waterway, Port, Coastal and Ocean Engineering, ASCE*, 118(3):249–266.

Heinrich, P., Piatanesi, A., and Hebert, H. (2001). Numerical modelling of tsunami generation and propagation from submarine slumps: the 1998 Papua New Guinea events. *Geophysical Journal International*, 145(1):97–111.

Heller, V. and Harger, W. H. (2010). Impulse product parameter in landslide generated impulse waves. *Journal of Waterway, Port, Coastal and Ocean Engineering, ASCE*, 136(3):145–155.

Heller, V. and Harger, W. H. (2011). Wave types of landslide generated impulse waves. *Ocean Engineering*, 38:630–640.

Heller, V., Harger, W. H., and Minor, H.-E. (2008). Scale effects in subaerial landslide generated impulse waves. *Experiments in Fluids*, 44(5):691–703.

Hirt, C. W. and Nichols, B. D. (1981). Volume of fluid (VOF) method for the dynamics of free boundaries. *Journal of Computational Physics*, 39:201–225.

Hoque, A. and Aoki, S. (2008). Air entrainment and associated energy dissipation in steady and unsteady plunging jets at free surface. *Applied Ocean Research*, 30(1):37 – 45.

Horrillo, J. J. (2006). *Numerical methods for tsunami calculation using full Navier-Stokes equations and the volume of Fluid method*. PhD thesis, University of Alaska, Fairbanks, Alaska.

Huber, A. (1980). Schwallwellen in seen als floge von felssturzen (reservoir impulse waves caused by rockfall), technical report mitteilung 47. Technical report, Laboratory of Hydraulics, Hydrology and Glaciology, Swiss Federal Institute of Technology, Zurich, Switzerland.

Huber, A. and Hager, W. H. (1997). Forecasting impulse waves in reservoirs. *Comminsion Internationale des Grands Barrages Barrages 19 Congress des Grand Barrages C Florence, Italy*, 31:993–1005.

Imamura, F. and Imteaz, M. M. A. (1995). Long waves in two-layers: governing equations and numerical model. *Science of Tsunami Hazards*, 14:13–28.

Imteaz, M. A. and Imamura, F. (2001). A non-linear numerical model for stratified tsunami waves and its application. *Science of Tsunami Hazards*, 19:150–159.

Iwasaki, S. (1983). Experimental study of a tsunami generated by a horizontal motion of a sloping bottom. *Bulletin of the Earthquakes Research Institute*, 57:239–262.

Jiang, L. and LeBlond, P. H. (1992). The coupling of a submarine slide and the surface waves which it generates. *Journal of Geophysical Research*, 97 (C8):12731–12744.

Jiang, L. and LeBlond, P. H. (1993). Numerical modeling of an underwater bingham plastic mudslide and the waves which it generates. *Journal of Geophysical Research*, 98 (C6):10303–10317.

Kamphuis, J. and Bowering, R. J. (1970). Impulse waves generated by landslides. *Proc. of 12th Coastal Engineering Conference, ASCE*, 1:575–588.

Koo, W. and Kim, M.-H. (2008). Numerical modeling and analysis of waves induced

by submerged and aerial/sub-aerial landslides. *KSCE Journal of Civil Engineering*, 12(2):77–83.

Kothe, D. B., Mjolsness, R. C., and Torrey, M. D. (1991). RIPPLE: A computer program for incompressible flows with free surces. Technical report, LA-12007-MS. Los Alamos National Laboratory, New Mexico.

Kowalik, Z., Horrillo, J. J., and Kornkven, E. (2005a). In Yeh, H., Liu, P. L.-F., and Synolakis, C., editors, *Advanced Numerical Models for Simulating Tsunami waves and Runup*, chapter Tsunami generation and runup due to 2D landslide, pages 269–272. World Scientific Publishing Co., New Jersey.

Kowalik, Z., Horrillo, J. J., and Kornkven, E. (2005b). In Yeh, H., Liu, P. L.-F., and Synolakis, C., editors, *Advanced Numerical Models for Simulating Tsunami waves and Runup*, chapter Tsunami runup onto a plane beach, pages 231–236. World Scientific Publishing Co., New Jersey.

Liu, P. L.-F., Wu, T.-R., Raichlen, F., Synolakis, C. E., and Borrero, J. C. (2005). Run-up and rundown generated by three-dimensional sliding masses. *Journal of Fluid Mechanics*, 536:107–144.

Lynett, P. and Liu, P. L.-F. (2005). A numerical study of the run-up generated by three dimensional landslides. *Journal of Geophysical Research*, 110, C03006:1–16.

Mader, C. and Gittings, M. L. (2002). Modeling the 1958 Lituya Bay mega-tsunami, ii. *Science of Tsunami Hazards*, 20(5):241–250.

Mader, C. and Gittings, M. L. (2003). Dynamics of water cavity generation. *Science of Tsunami Hazards*, 21(2):91–101.

Miller, D. J. (1960). Giant Waves in Lituya Bay, Alaska. *Geological Survey Professional Paper*, 354-C. U.S. Government Printing Office, Washington DC.

Miller, D. J. (1970). Prediction curves for waves near the source of an impulse. *Proc. of 12th Coastal Engineering Conference*, 12:609–624.

Mohammed, F. (December 2010). *Physical Modeling of Tsunami Generated By Three-dimensional Deformable Granular Landslides*. PhD thesis, Georgia Institute of Technology, Georgia.

Mohammed, F., McFall, B. C., and Fritz, H. M. (2011). Tsunami generation by 3D deformable granular landslides. *Solutions to Coastal Disasters 2011, ASCE*, Proceedings of the 2011 Solutions to Coastal Disasters Conference:310–320.

Monaghan, J. J. (1992). Smoothed particle hydrodynamics. *Annual review of astronomy and astrophysics*, 30 (A93-25826 09-90):543–574.

Monaghan, J. J. and Kos, A. (2000). Scott Russell's wave generator. *Physics of Fluids*, 12(3):622–630.

Montagna, F., Bellotti, G., and Di Risio, M. (2011). 3D numerical modeling of landslide-generated tsunami around a conical island. *Natural Hazards*, 58:591–608.

Morse, P. M. and Feshbach, H. (1953). *Methods of Theoretical Physics*. McGraw-Hill, New York.

Müller (1964). The rock slide in the vajont valley. *Rock Mechanism and Engineering Geology*, 2:148–212.

Nichols, B. D., Hirt, C. W., and Hotchkiss, R. S. (1980). SOLA-VOF: A solution algorithm for transient fluid flow with multiple free boundaries. Technical report, LA-8355, Los Alamos National Laboratory, New Mexico.

Noda, E. K. (1970). Water waves generated by landslides. *Journal of the Waterways, Harbors and Coastal Engineering Division, ASCE*, 7699, WW4:835–855.

Panizzo, A., Bellotti, G., and De Girolamo, P. (2002). Application of wavelet transform analysis to landslide generated waves. *Coastal Engineering*, 44(4):321–338.

Panizzo, A., De Girolamo, P., Di Risio, M., Maistri, A., and Petaccia, A. (2005a). Great landslide events in italian artificial reservoir. *Natural Hazards and Earth System Science*, 5:733–740.

Panizzo, A., De Girolamo, P., and Petaccia, A. (2005b). Forecasting impulse waves generated by subaerial landslides. *Journal of Geophysical Research*, 110, C12025:23.

Russell (1838). Report of the committee on waves. *Rep. 7th Meeting British Association Advanced Science, Liverpool*, 1837:417–496.

Russell (1845). Report on Waves. *14th Meeting British Association Advanced Science*, 1844:311–390.

Savage, S. B. and Hutter, K. (1989). The motion of a finite mass of granular material down a rough incline. *Journal of Fluid Mechanics*, 199:177–215.

Schwaiger, H. F. and Higman, B. (2007). Lagrangian hydrocode simulations of the 1958 Lituya Bay tsunamigenic rockslide. *Geochemistry, Geophysics, Geosystems*, 8(Q07006):1–7.

Silva, R., Losada, I. J., and Losada, M. A. (2000). Reflection and transmission of tsunami wave by coastal structures. *Journal of Applied Ocean Research*, 22:215–223.

Swanson, R. C. and Jones, W. T. (1982). Mudslide effects on offshore pipelines. *Transportation Engineering Journal*, 108:585–600.

Synolakis, C. E., Bardet, J., Borrero, J. C., Davies, H. L., Okal, E. A., Silver, E. A., Sweet, S., and Tappin, D. R. (2002). The slump origin of the 1998 Papua New Guinea Tsunami. *Proceedings of the Royal Society of London, Series A*, 458:763–789.

Synolakis, C. E., Bernard, E. N., V., T. V., Kanoglu, U., and Gonzalez, F. I. (2007). Standards, criteria, and procedures for noaa evaluation of tsunami numerical models. Technical Report NOAA Tech. Memo. OAR PMEL-135, NOAA/Pacific Marine Environmental Laboratory, Seattle, WA.

Tappin, D. R., Watts, P., McMurtry, G. M., Lafoy, Y., and Matsumoto, T. (2001). The sissano, Papua New Guinea tsunami of july 1998 - 0ffshore evidence on the source mechanism. *Marine Geology*, 175(1-4):1–23.

Walder, J. S., Watts, P., Sorensen, O. E., and Janssen, K. (2003). Tsunamis generated by subaerial mass flows. *Journal of Geophysical Research*, 108(B5):2236, 19pp.

Watts, P., Grilli, S., Kirby, J. T., Fryer, G. J., and Tappin, D. R. (2003). Landslide tsunami case studies using a Boussinesq model and a fully nonlinear tsunami generation model. *Natural Hazards Earth System Science*, 3:391–402.

Watts, P., Grilli, S. T., Tappin, D. R., and Fryer, G. J. (2005). Tsunami generation

by submarine mass failure. i: predictive equations and case studies. *Journal of Waterway, Port, Coastal and Ocean Engineering, ASCE*, 131(6):298–310.

Watts, P., Imamura, F., and Grilli, S. (2000). Comparing model simulations of three benchmark tsunami generation cases. *Science of Tsunami Hazards*, 18(2):107–123.

Welch, S., Trapp, J., and Mortensen, G. (1994). Interface tracking in two-phase flow simulations using a simple subgrid counting procedure. *Proceedings of the 1994 ASME Summer Symposium on Numerical Methods in Multiphase Flows*, FED 185:293–299.

Wiegel, R. L. (1955). Laboratory studies of gravity waves generated by the movement of a submerged body. *Berkeley : University of California. Institute of Engineering Research. Wave Research Laboratory*, 36(5):759–774.

Wiegel, R. L., Noda, E. K., Kuba, E. M., Gee, D. M., and Tornberg, G. F. (1970). Water waves generated by landslides in reservoir. *Journal of the Waterways, Harbors and Coastal Engineering Division, ASCE*, 96(WW2):307–333.

Yim, S. C., Yuk, D., Panizzo, A., Di Risio, M., and Liu, P.-F. (2008). Numerical simulation of wave generation by a vertical plunger using rans and SPH models. *Journal of Waterway, Port, Coastal and Ocean Engineering, ASCE*, 134(3):143–159.

Zweifel, A. (2004). *Impulswellen: Effekte der Rutschdichte und der Wassertiefe*. PhD thesis, ETH Zurich, Zurich (in German).

Zweifel, A., Harger, W. H., and Minor, H.-E. (2006). Plane impulse waves in reservoirs. *Journal of Waterway, Port, Coastal and Ocean Engineering, ASCE*, 132(5):358–368.

APPENDIX A

Snapshot for boundary conditions, meshing, and geometry set-up for FLOW-3D

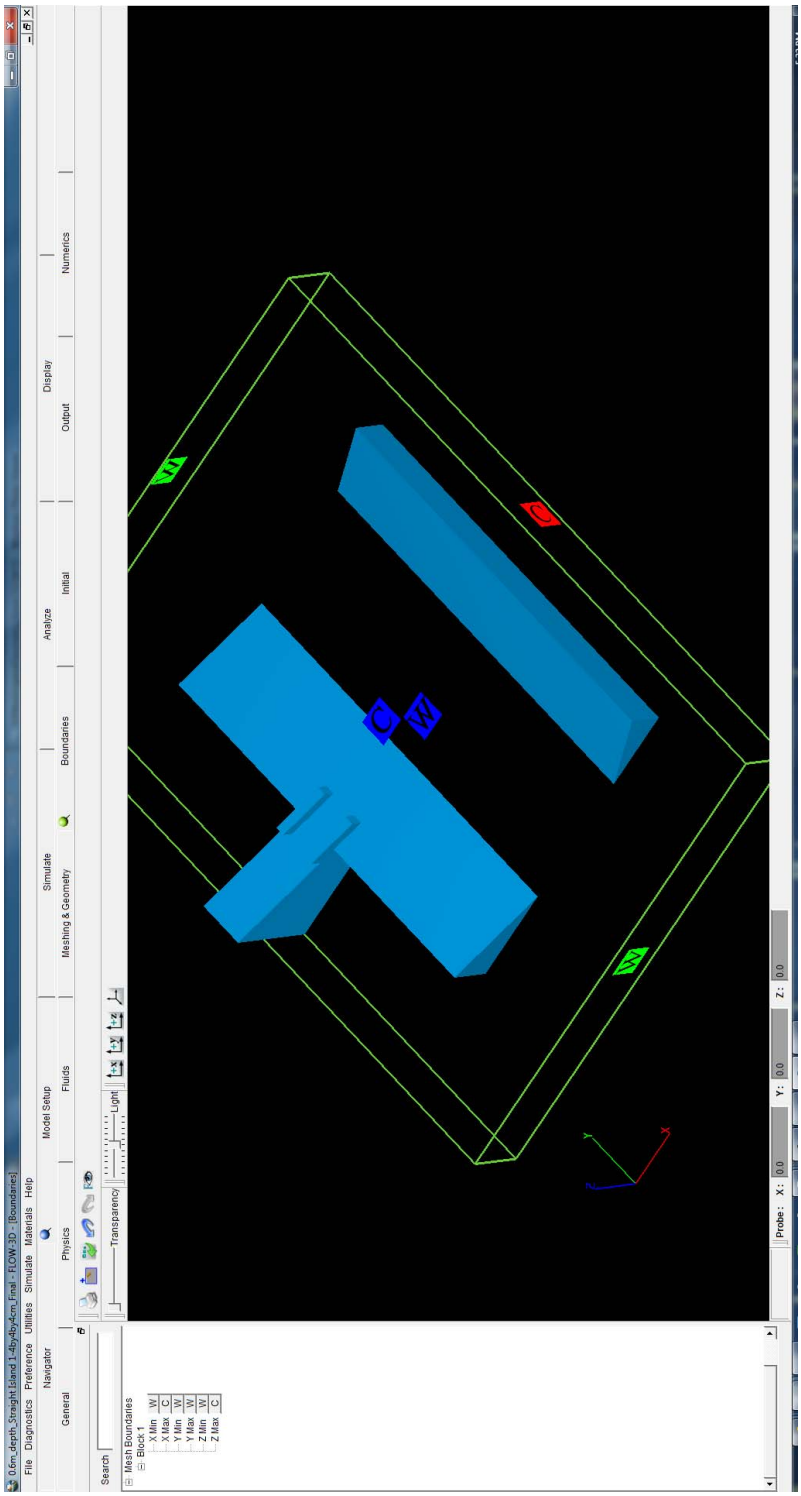

Figure A.1: Configurations of boundary conditions for fjord case: FLOW-3D

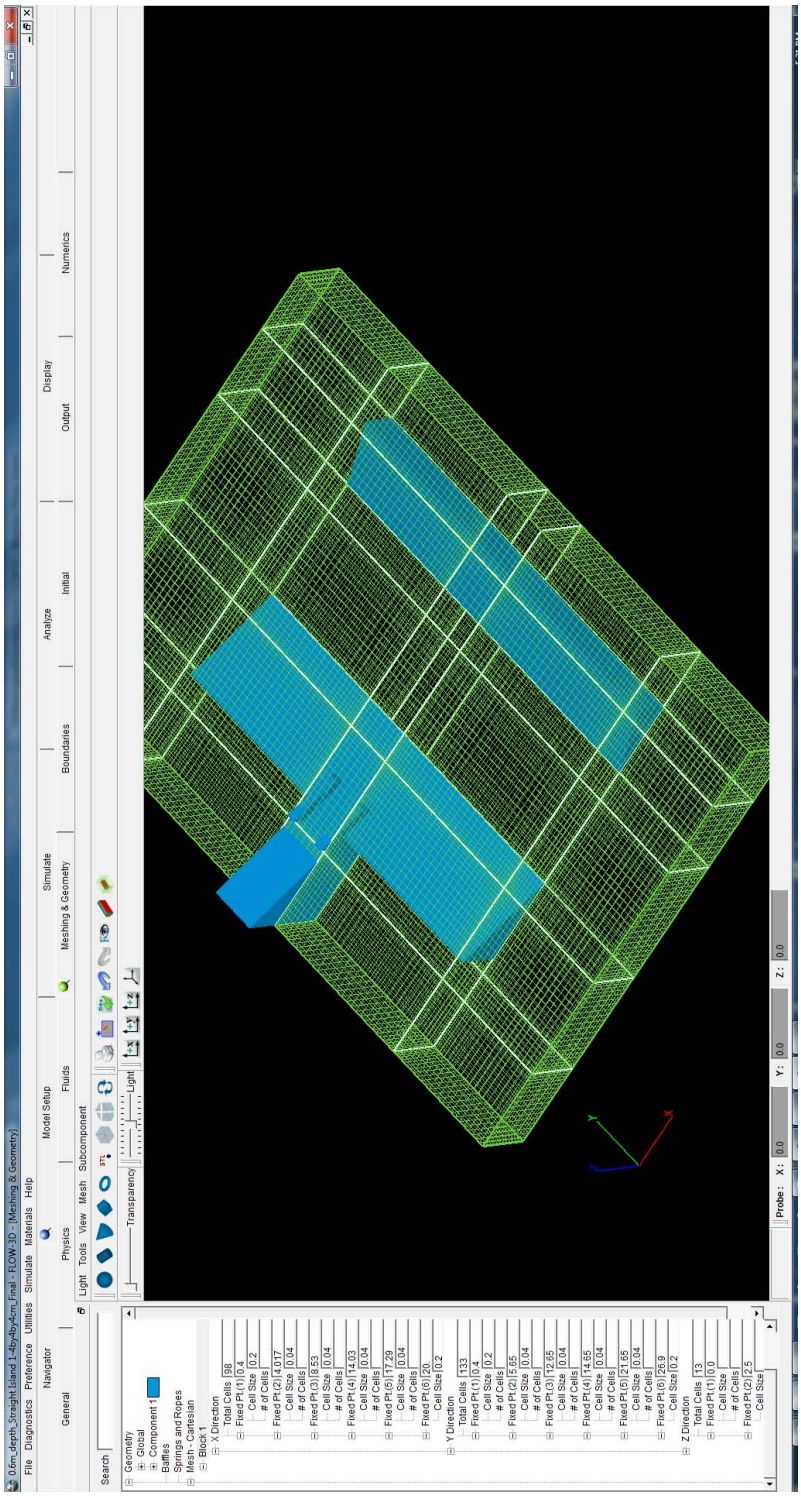

Figure A.2: 3D meshing and geometry for fjord case: FLOW-3D

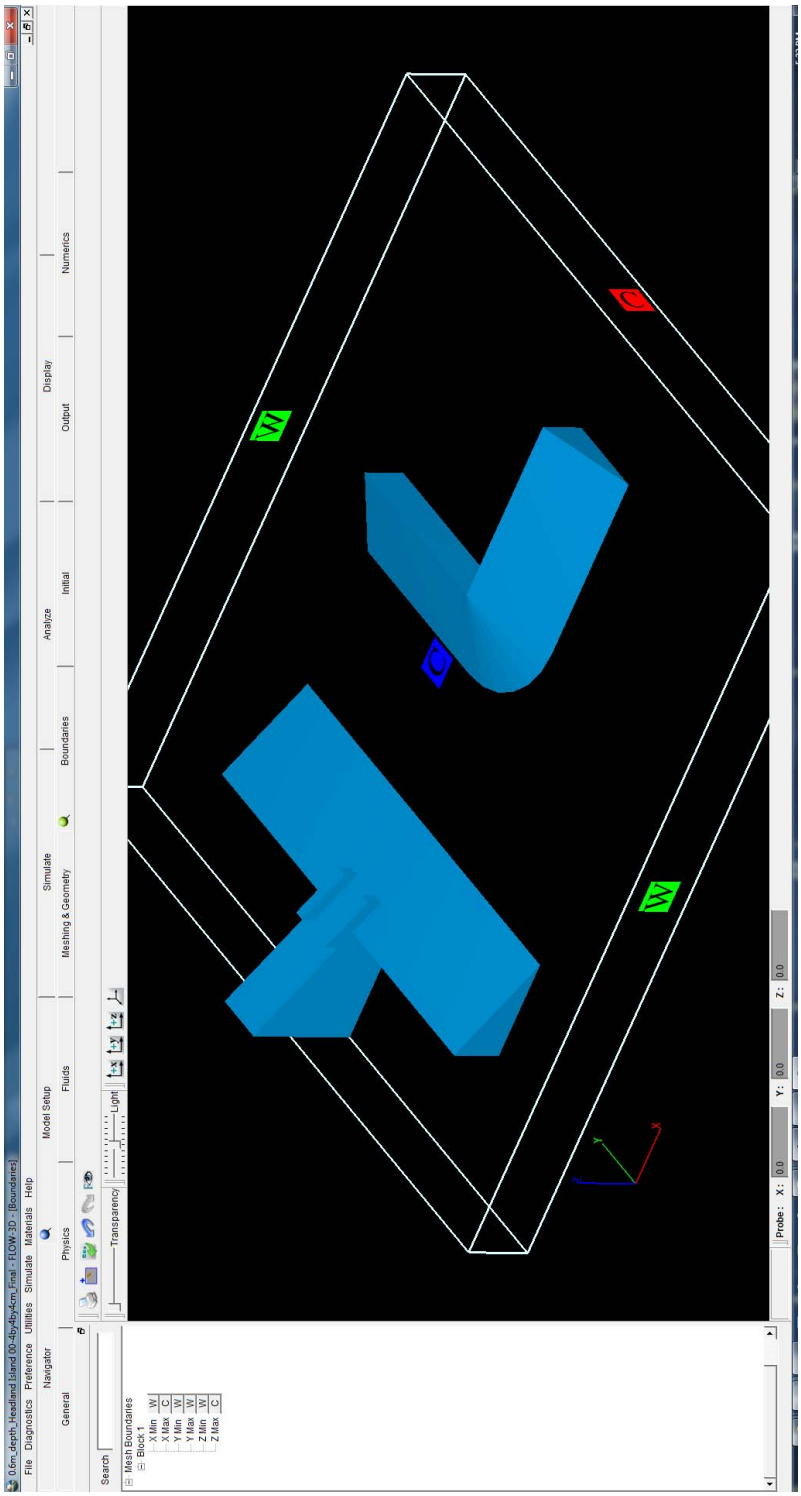

Figure A.3: Configurations of boundary conditions for headland case: FLOW-3D

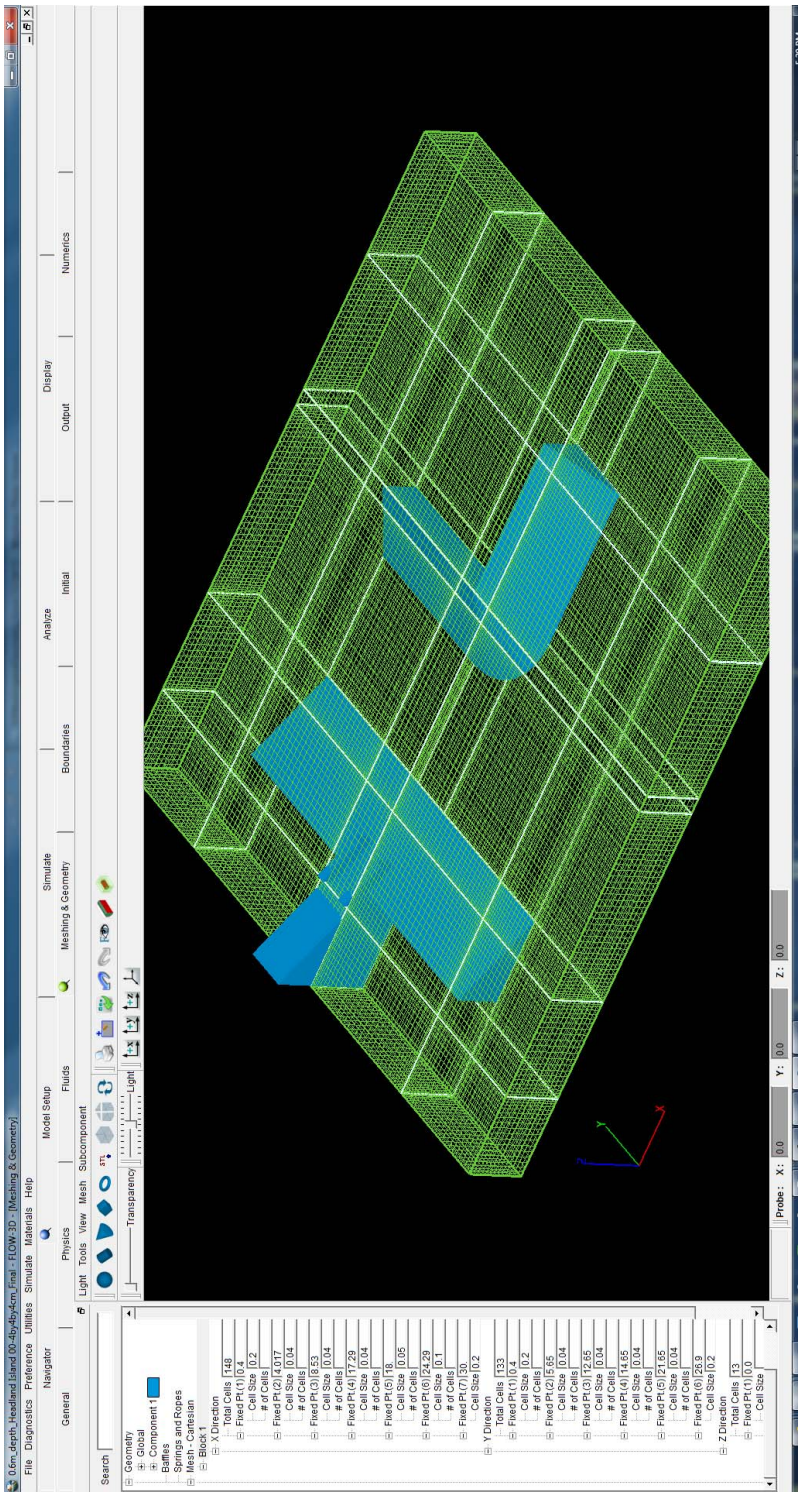

Figure A.4: 3D meshing and geometry for headland case: FLOW-3D

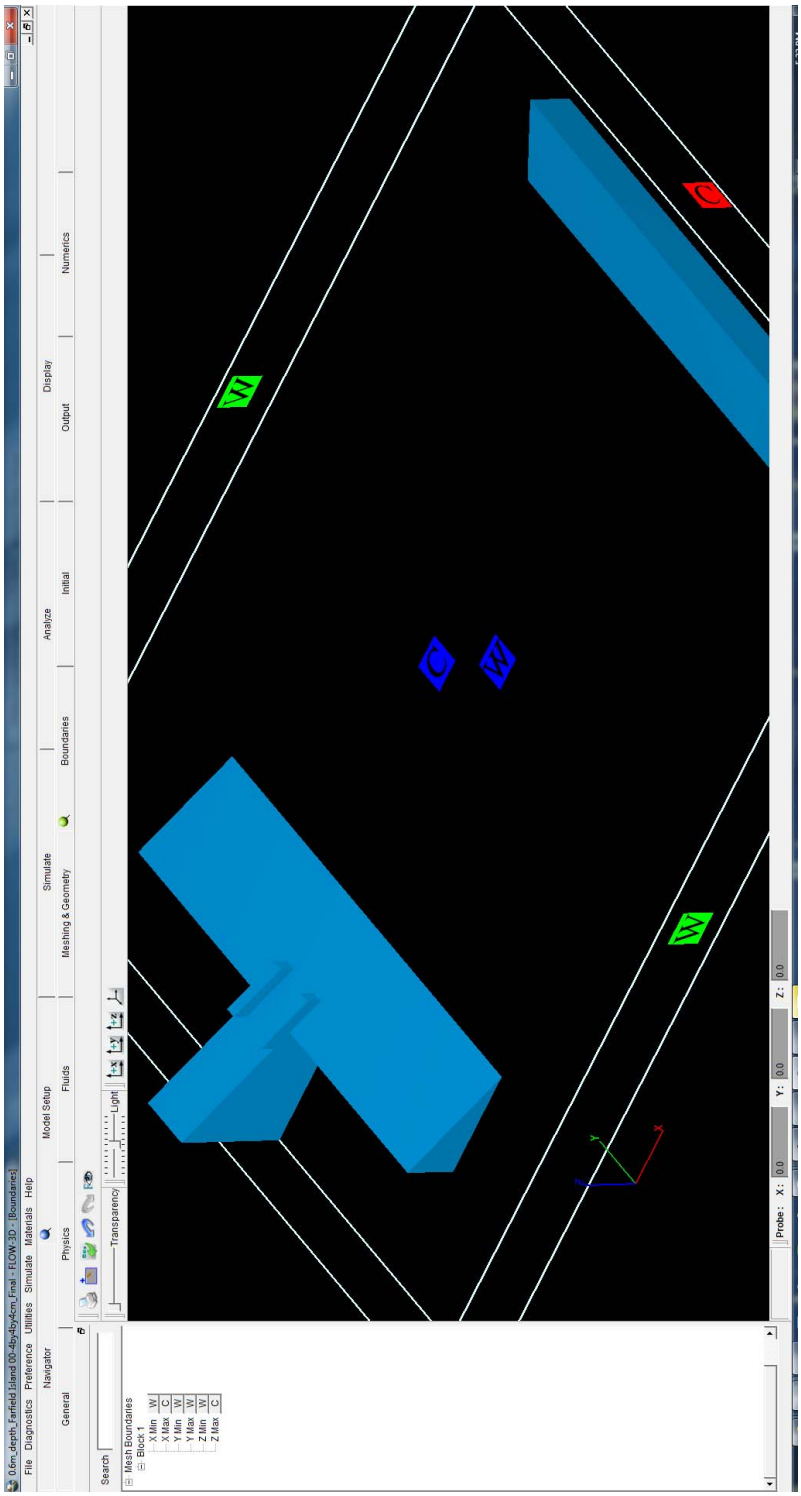

Figure A.5: Configurations of boundary conditions for farfield case: FLOW-3D

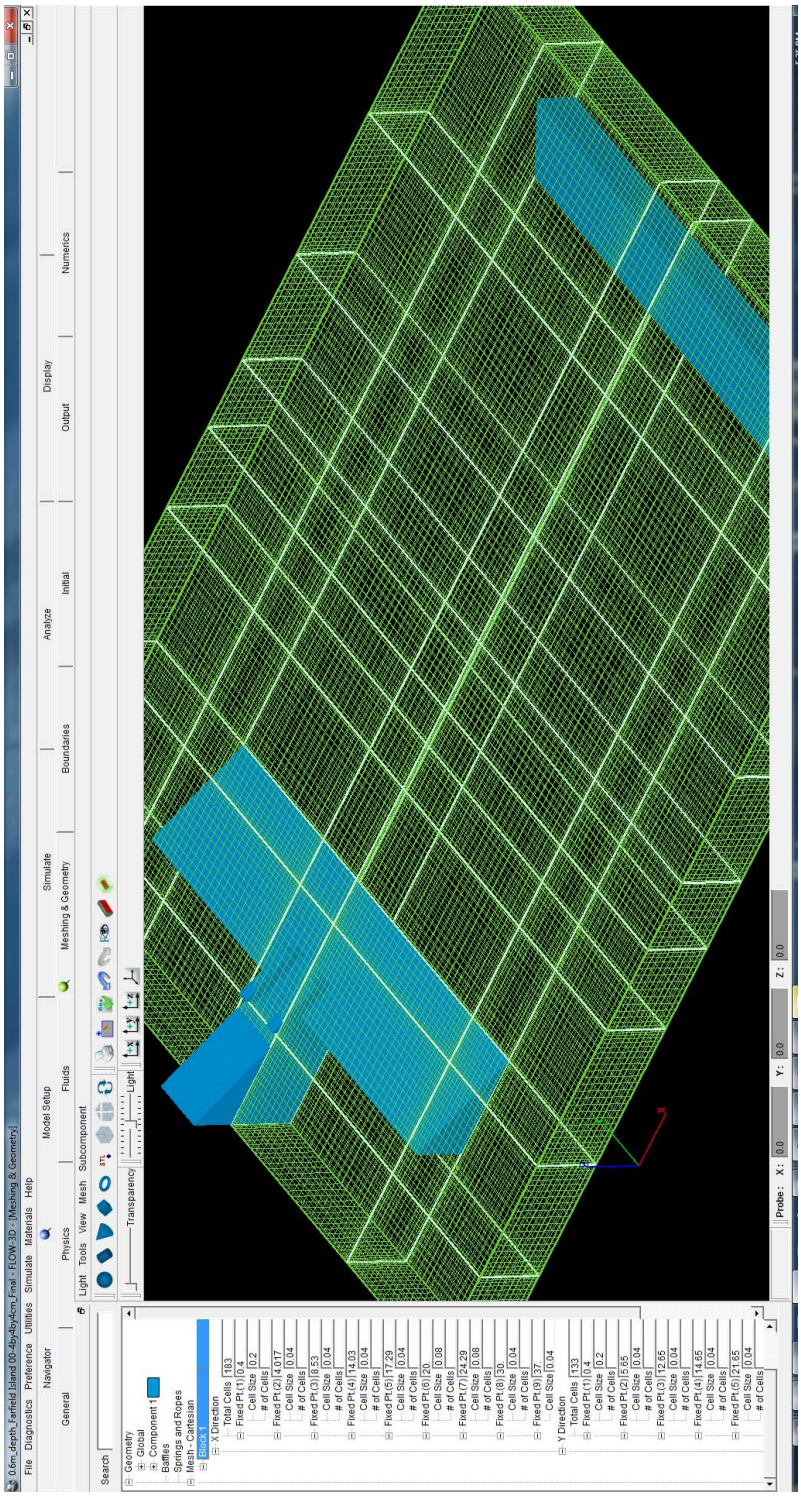

Figure A.6: 3D meshing and geometry for farfield case: FLOW-3D